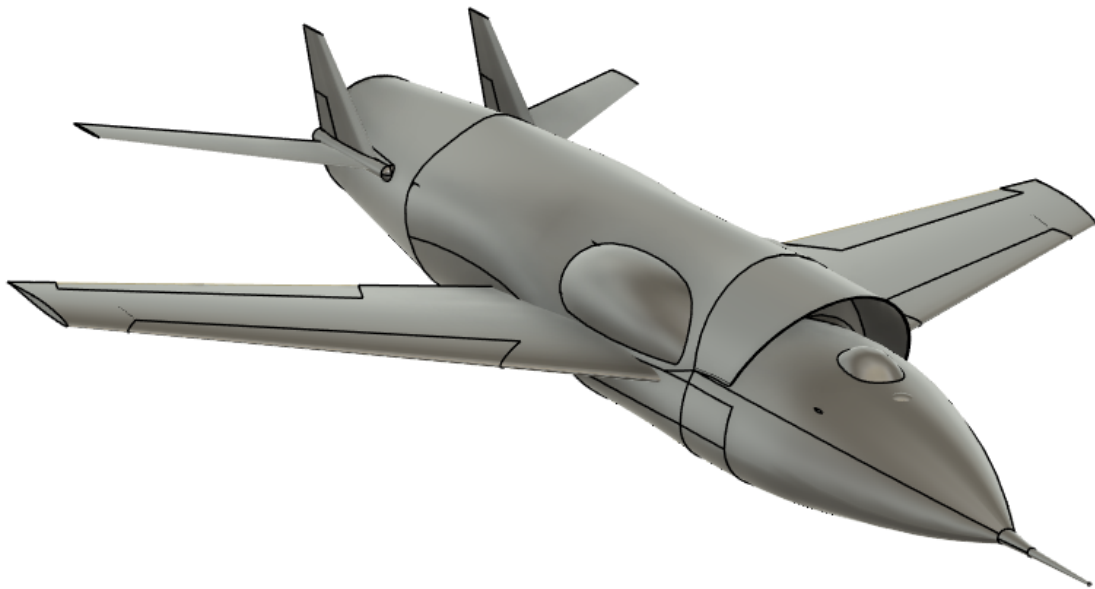


# Aerosp 481 Team 03: Libellula PDR Report



## Authors:

Niko Economos  
Shaylin Ciaramitaro  
Joon Kyo Kim  
Juan Esteban Vega  
Vienna Chafart  
Victoria Cobb

*University of Michigan, Aerospace Engineering*

# Contents

<b>I Summary</b>	<b>4</b>
I.A Executive Summary . . . . .	4
I.B 3D Design View . . . . .	5
I.C Performance Parameters . . . . .	7
<b>II Introduction</b>	<b>8</b>
<b>III Configuration</b>	<b>9</b>
<b>IV Preliminary Sizing</b>	<b>10</b>
IV.A Initial Weight Estimate . . . . .	10
IV.B T/W vs W/S . . . . .	11
IV.C Improved Weight Estimate . . . . .	12
IV.D $T$ vs $S$ with objective function . . . . .	13
<b>V Interior Layout</b>	<b>14</b>
V.A Interior Components . . . . .	14
V.B Component Weights and Aircraft Balance . . . . .	15
<b>VI Stability and Control</b>	<b>15</b>
<b>VII Aerodynamics</b>	<b>18</b>
VII.A Wing Design . . . . .	18
VII.A.1 Wing Area . . . . .	18
VII.A.2 Aspect Ratio . . . . .	18
VII.A.3 Span . . . . .	19
VII.A.4 Taper Ratio . . . . .	19
VII.A.5 Wing Incidence And Twist . . . . .	19
VII.A.6 Sweep . . . . .	20
VII.A.7 Wing Configuration . . . . .	20
VII.A.8 High Lift Devices . . . . .	21
VII.B Airfoil Selection . . . . .	22
VII.C Stall Speed . . . . .	23
VII.D Empennage Configuration . . . . .	23
VII.D.1 Vertical Tail . . . . .	23
VII.D.2 Horizontal Tail . . . . .	24
VII.E Airfoil Selection . . . . .	25
VII.E.1 Vertical Tail . . . . .	25
VII.E.2 Horizontal Tail . . . . .	25
VII.F Dimensions After Volume Coefficient Based Sizing and Airfoil Selection . . . . .	25
<b>VII Method Validation</b>	<b>26</b>
<b>IX Objective Function</b>	<b>26</b>
<b>X Propulsion System</b>	<b>28</b>
<b>XI Government Furnished Equipment</b>	<b>28</b>
<b>XII Computational Procedure and Software Design</b>	<b>30</b>
XII.A Initialization, Initial TOGW Estimate, and T/W and W/S Constraint Mapping . . . . .	31
XII.B Finding $T$ , $S$ , and Updated TOGW Estimate . . . . .	32
XII.C Refined Weight & Aerodynamic Estimates . . . . .	33

<b>XIII</b> Conclusions	<b>33</b>
<b>XIV</b> References	<b>34</b>
<b>XV</b> Appendix	<b>36</b>
XV.AConstraint Equations	36
XV.A.1 $\frac{W}{S}$ Constraint from Landing Field Length	36
XV.A.2 $\frac{T}{W}$ Takeoff Field Length	36
XV.A.3 $\frac{W}{S}$ Instantaneous Turn	37
XV.A.4 $\frac{T}{W}$ Sustained Turn	37
XV.A.5 $\frac{T}{W}$ Cruise and Dash	37
XV.A.6 $\frac{T}{W}$ Ceiling	38
XV.A.7 $\frac{T}{W}$ Climb	38
XV.A.8 $\frac{T}{W}$ Specific Excess Power	38
XV.BAdditional Equations	39
XV.B.1 Empty Weight Fraction Regression	39
XV.B.2 $S_{wet}$ from TOGW Regression	39
XV.CAdditional Plots	39
XV.DWing Parameters	40
XV.EWing Design	41
XV.FEmpennage Design	42

## I. Summary

### A. Executive Summary

With increasing tensions across the globe, the AIAA has launched an Undergraduate Team Design Challenge to design an aircraft that meets these emerging security concerns. The design is to be a homeland defense interceptor, capable of completing three specified missions. Key requirements include a cost cap of \$25M per aircraft for a 1000 unit purchase and readiness for operational deployment by 2027.

The aircraft design prioritizes mission success by incorporating features that enhance speed, maneuverability, and stealth. The proposed interceptor features a single engine, highly swept back wing, and a twin tail configuration to optimize aerodynamic performance. The design also features remote pilot capabilities to reduce cost and eliminate the weight associated with crew and life support systems, while also taking into account safety concerns that may have arose with a piloted aircraft.

The fuselage is designed to optimize aerodynamic efficiency, stealth, and internal capacity. It features a rounded nose, which minimizes drag and improving overall aerodynamic performance. The top-mounted inlet is strategically placed to ensure unobstructed airflow to the single engine, reducing the likelihood of foreign object damage and contributing to a low radar cross-section. This positioning is highly unconventional for a frontline military aircraft, but helps show the versatility of the overall design. An internal weapons bay is integrated into the fuselage, allowing for munitions to be carried without compromising the stealth of the aircraft during missions. This configuration also helps reduces the external drag typically associated with missiles mounted on wing launchers. The single engine design enables a more compact fuselage configuration, reducing weight and contributing to a large  $T/W$  ratio. The internal volume was maximized in this design in order to allow for advanced avionics, fuel storage, ammunition, and other mission-specified equipment.

The wing is designed to optimize the maneuverability, efficiency, and structural integrity of the aircraft. It features a highly swept-back wing configuration to reduce wave drag at transonic speeds. The mid-wing configuration minimizes interference drag, enhances performance at high G's and rapid maneuvers, and avoids ground clearance issues faced by low-wing designs and roll over-stability faced by high-wing designs. The wing utilizes a thin airfoil—the NACA 64A-206—due to our aircraft's similarity to the F-16, but is currently being reconsidered due to potential performance concerns. For high lift devices, we are incorporating leading edge extensions (currently under refinement), flaperons, and leading edge flaps. These features aim to simplify the overall design, thus reducing cost and weight, while also increasing the lift generated.

The empennage is designed to provide stability, control, and stealth, with a configuration that enhances the aircraft's overall aerodynamic performance. It features a twin tail design, which allows for better control authority of the aircraft, and isolates yaw actuation to simplify the flight dynamics. This configuration helps to reduce developmental costs by minimizing time spent in test flights. The horizontal tails were positioned to reduce the aerodynamic interference from the wings and fuselage, thus ensuring reliable pitch control, especially during aggressive maneuvers or low speeds.

While this design has reached maturity for this stage of design, significant work remains before it can proceed to manufacturing and operational deployment. Our immediate next steps include refining our current design and preparing for the detailed design phase. Key actions include re-evaluating the selected airfoil for the wings, and the refinement and CAD integration of the leading edge extensions. Additionally, we will focus on iterative testing to identify further areas for improvement.

Ultimately, our aircraft design represents a significant advancement in homeland defense capabilities, aligning with the specified requirements of the AIAA Undergraduate Team Design Challenge. By integrating cutting-edge technologies and prioritizing aerodynamic efficiency, stealth, and operational flexibility, we are poised to deliver a high-performance interceptor that meets both budgetary and timeline constraints given within the competition requirements. As we progress into the detailed design phase, our focus will remain on iterative refinement and validation, ensuring that we achieve the highest standards of performance and safety. We are striving to create a system that not only fulfills its intended missions, but also sets a new benchmark for future military aircraft designs.

## B. 3D Design View

A Three-view drawing and perspective view of our aircraft is shown in the figure below. The views indicate the general dimensions of the aircraft, the center of gravity and neutral point, locations for control surfaces, and weapon stowage. In consideration of the neutral point, the derivation of which is discussed in the Stability and Control Section VI, different Mach numbers were considered; in this section, the fully-loaded condition at cruise ( $M = 0.85$ ) and the fully-expended condition at landing ( $M = 0.28$ ) will be discussed. The center of gravity was calculated to be around 10.185 m aft of the tip of the nose in the fully loaded condition. At cruise, the neutral point sits just after this point, at around 10.310 m aft of the nose tip. This places our loaded aircraft at a static margin of 4.0%, a region of weak stability.

Also indicated in the drawings are the preliminary landing gear positions, which place the aircraft around 1 meter off the ground. The landing gear constraint angles are outlined in Table 1:

**Table 1 Landing Gear Constraint Angles**

Parameter for Loaded Aircraft	Value
Rotation Angle Clearance	14.33°
Tipback Angle	36.09°
Tipover Angle Clearance	25.71°
Overtake Angle	40.36°

The rotation clearance and tipback angles are satisfactory considering a maximum rotation angle of 13 degrees between takeoff and landing. The overtake angle is also satisfactory according to the absolute maximum constraint of 60 degrees.

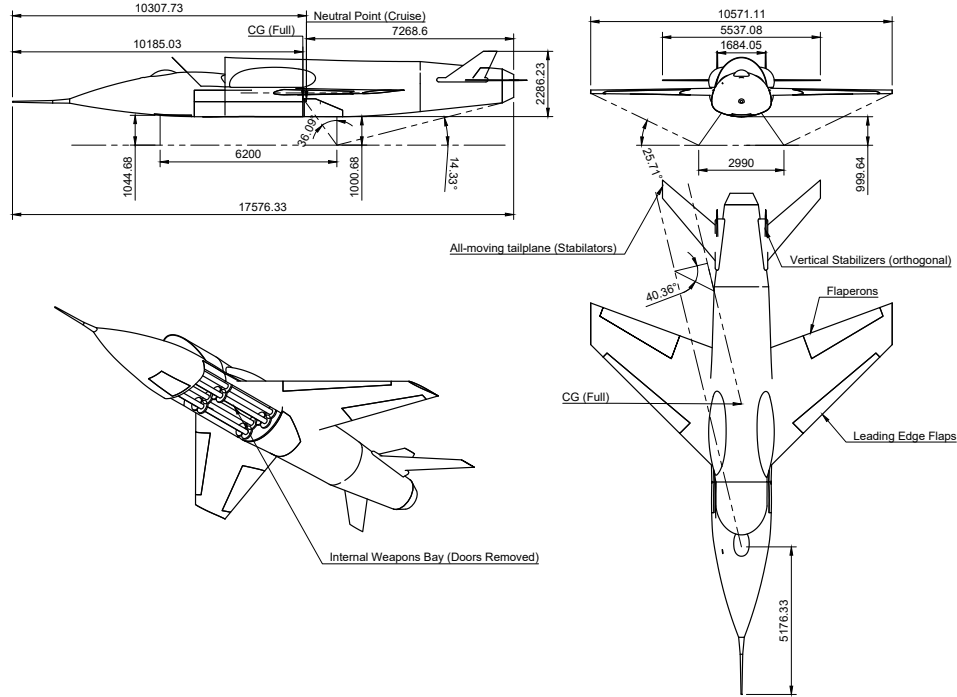


**Fig. 1 Three-view and perspective drawing of the aircraft in the fully loaded condition**

As the aircraft deploys payload, the static margin was shown to shift to negative values. The center of gravity moves backwards, to 10.794 m aft of the nose tip. The neutral point at landing speed moves a small amount to 10.280 m, placing the static margin at around -16.9%, a region of moderate instability, which will necessitate the integration of a flight control system. Our aircraft has sufficient internal volume for an additional system, and considering most

frontline fighter aircraft currently in service integrate some form of a flight control computer to facilitate enhanced maneuverability, this will not detrimental to our design. The landing gear constraint angles for this case are outlined in Table 2.

**Table 2 Landing Gear Constraint Angles**

Parameter for Unloaded Aircraft	Value
Rotation Angle Clearance	14.33°
Tipback Angle	21.98°
Tipover Angle Clearance	25.71°
Overtake Angle	37.48°

Even with the decreased constraint angles, they remain within the acceptable bounds, and are thus valid for our design.

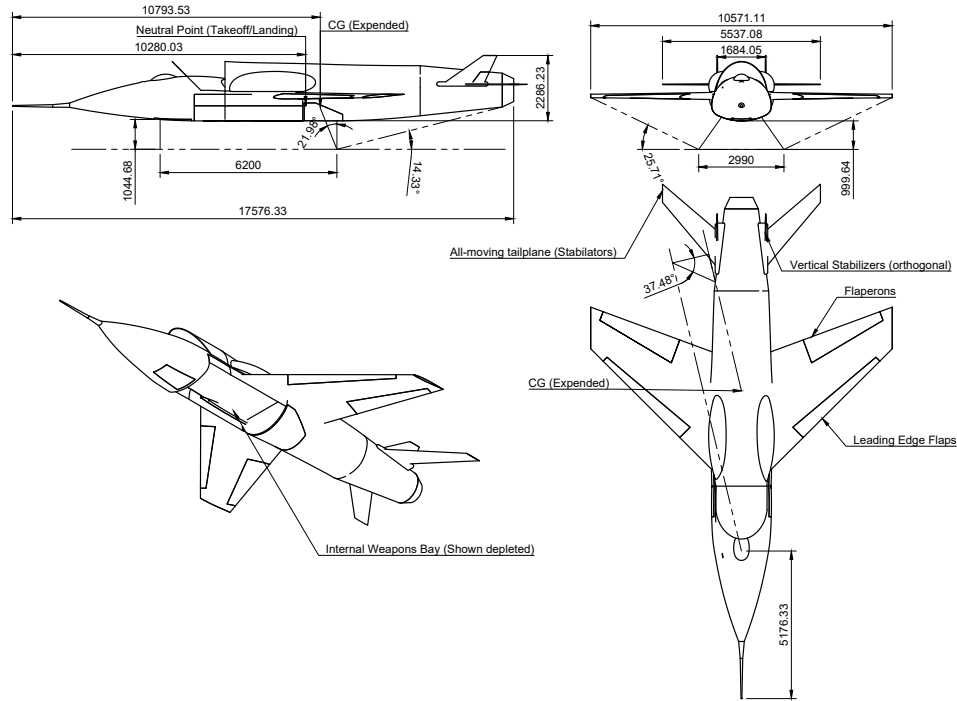


**Fig. 2 Three-view drawing of the aircraft in the payload expended condition**

## C. Performance Parameters

**Table 3 Performance Parameters**

Parameter	Our Aircraft	F-35A	F-16	F-22
Takeoff Weight (lbs)	27,558	70,000	37,500	83,500
Empty Weight (lbs)	13,800	29,300	18,900	43,340
Payload (lbs)	2,822	18,000	17,000	20,000
Number of Missiles	6	6	6	6
Cruise, Takeoff, Landing $C_L$	1.25, 1.70, 2.00	0.6, 1.4, 1.9	0.4, 1.2, 1.7	0.5, 1.3, 1.8
Cruise $L/D$	9.485	15	10	8.4
$T/W$ max (hp/lbs)	1.05	1.1	1.3	1.8
$W/S$ (lbs/ft <sup>2</sup> )	108	152	125	99
Engine type & max SLS thrust	F110-GE-129, 129 kN	F135-PW-100, 191 kN	F100-PW-200*, 89 kN	F119-PW-100, 311 kN
Engine cruise SFC (kg/N/h)	0.067	0.9-1.0	0.78-0.85	0.9
Span (ft)	28.5	35	32.8	44.5
Reference Area (ft <sup>2</sup> )	264	460	300	840
Aspect ratio	3.07	2.66	3.59	2.36
Average wing $t/c$	6%	-	-	-
Cruise Mach no. (Max and Economic)	1.6, 0.85	1.6, 0.85	2.0, 0.8	2.25, 0.85
Maximum range (nm)	3.03E+06	1,380	2,280	1,839
Maximum range fuel burn (kg)	10,714	11,000	8,500	12,000
Payload**	6x AIM-120, 1x M61A1	4x AIM-120, 2x AIM-9	2x 2,000 lb bombs, 2x AIM-9, 2x AIM-120, 2x 2,400 lbs external tanks	2x 1,000 lb GBU-32, 2x AIM-120, 2x AIM-9
Static margin	0.04	-0.102	-0.02	-
Maximum landing distance (ft)	26,247	8,000	2,953	8,000
Maximum takeoff distance (ft)	26,247	8,000	3,609	1,575
Avg. flyaway cost for 250, 500, & 1000 units (USD)	16.1M, 14.6M	15.3M, 14.6M	100M, 80M, 70M	30M, 25M, 20M
				150M, 120M, 100M

\*Multiple engines available

\*\*Multiple configurations available

## II. Introduction

Due to rising geopolitical tensions, we were tasked with designing a Homeland Defense Interceptor (HDI) aircraft that is agile, cost-effective and dedicated to defending U.S. airspace. Our design seeks to fill a crucial gap left by current Air Force and Navy fighter fleets, which are too expensive to field in sufficient numbers for the intended missions. The goal of this project is to provide an affordable, high-performance solution that ensures sufficient homeland defense coverage without diverting funds from offensive force capabilities.

Our HDI aircraft will support three core mission profiles, each with distinct operational demands. The primary, and most constraining, is the Defensive Counter-Air mission, which requires extensive fuel capacity due to its endurance and range demands, resulting in a higher overall weight necessary for the aircraft. Additionally, the HDI aircraft will complete a point defense intercept mission, focused on high-speed, short duration interceptions, and an intercept and escort mission for protecting other aircraft over a set range. Depictions of each mission profile are provided in Figures 3, 4, and 5. These missions collectively define the operational flexibility necessary to counter diverse airspace threats while maintaining budgetary and logical feasibility.

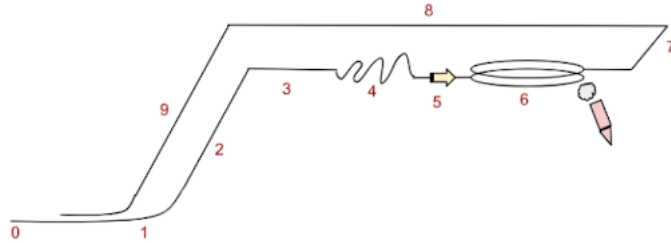


**Fig. 3 Defensive Counter-Air Patrol Mission Profile**

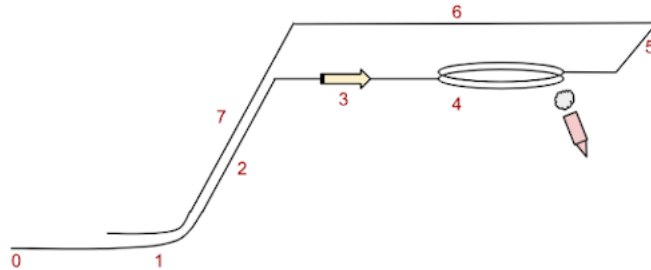


**Fig. 4 Point Defense Intercept Mission Profile**

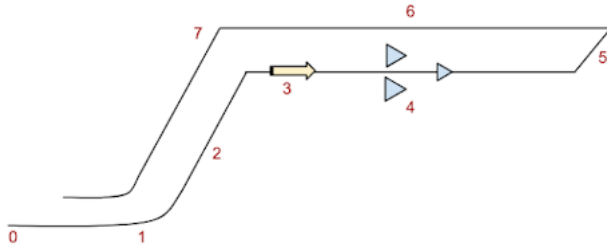


**Fig. 5 Intercept and Escort Mission Profile**

Our design and performance requirements are centered around cost-effectiveness and operational efficiency. The HDI must be remotely piloted, removing the need for an onboard pilot, and allowing for a smaller, streamlined airframe. To ensure we meet the budget constraint of staying below 25 million dollars per aircraft, the design will incorporate practical measures to reduce complexity and streamline maintenance capabilities. The HDI will operate in all weather conditions and from standard NATO runways, making it adaptable to various environments and ready for rapid deployment by 2027. A further breakdown of the design requirements is provided in Figure 6.

Additionally, the HDI is designed to meet rigorous performance standards necessary for effective homeland defense.

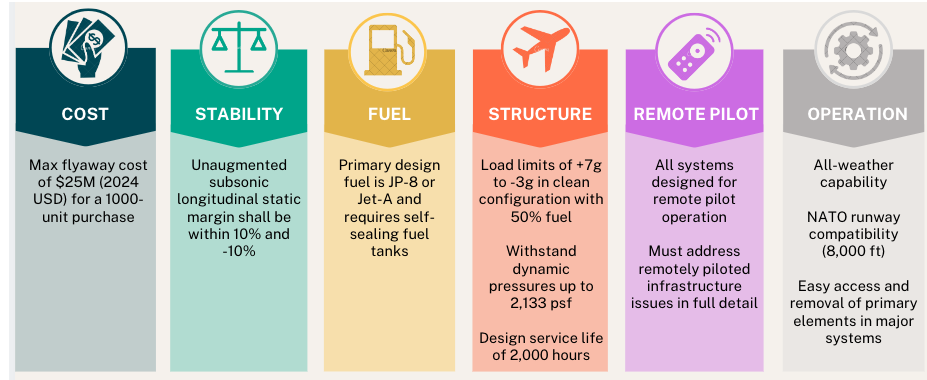


**Fig. 6 Design Requirements of the Aircraft**

It must achieve a maximum mach number of 1.6 at an altitude of 35,000 feet, allowing it to intercept and engage high-speed threats swiftly. Specific excess power requirements are set for various altitudes and speeds, ensuring strong acceleration and climb capabilities essential for both immediate threat response and sustained combat maneuvers. The aircraft must sustain a load factor up to 5 G's under maximum thrust conditions, enabling sharp turns and agile responses during high-stakes engagements. Furthermore, the HDI must meet endurance requirements for long-range missions, such as maintaining combat air patrol for hours at a 300 nm radius. A more detailed breakdown of the performance requirements the HDI must meet are provided in Figure 7. These performance capabilities ensure that the HDI can efficiently patrol, intercept, and neutralize a range of airborne threats, enhancing the security of U.S. airspace.

Mission Performance	<ul style="list-style-type: none"> <li>Intercept mission radius of 200 nm</li> <li>DCA combat air patrol endurance of 4 hours at a 300 nm radius from base</li> </ul>
Performance at Maneuver weight (50% internal fuel)	<ul style="list-style-type: none"> <li>Max Speed of M = 1.6 at 35,000 ft</li> <li>Maximum Instantaneous Turn Rate at 35,000 ft is 18.0 deg/s</li> <li>Military Thrust: <ul style="list-style-type: none"> <li>1-g Specific Excess Power - 200 ft/s (SL) and 50 ft/s (15,000 ft)</li> </ul> </li> <li>Maximum Thrust: <ul style="list-style-type: none"> <li>1-g Specific Excess Power - 700 ft/s (SL) and 400 ft/s (15,000 ft)</li> <li>5-g Specific Excess Power - 300 ft/s (SL) and 50 ft/s (15,000 ft)</li> <li>Sustained load factor of 5.0 g's at 15,000 ft</li> </ul> </li> </ul>

**Fig. 7 Summary of Performance Requirements of the Aircraft**

### III. Configuration

In designing the Homeland Defense Interceptor aircraft, the primary objective is to minimize costs while creating a compact, straightforward design that meets mission requirements for maneuverability, endurance, and armament capacity. To achieve this, we have prioritized a minimalist design philosophy, ensuring the aircraft is as small and lightweight as possible while maintaining sufficient storage for essential weapons, equipment, and fuel. Given the high maneuverability demands in our Defensive Counter-Air Patrol and Point-Defense Interception missions, our configuration is designed to be moderately unstable for later phases of flight. This slight instability enhances agility, as seen in many advanced fighter designs, which utilize controlled instability to meet high maneuverability requirements. Further analysis of stability and control specifics has been covered in II.B which covers the 3-D design of the aircraft.

Our interior storage is engineered to carry six AIM-120 missiles internally. The choice of six missiles was carefully balanced to meet operational requirements for effective air-to-air protection without unnecessarily increasing the aircraft's weight or complexity. Storing the missiles internally reduces drag and enhances the aircraft's stealth profile and overall aerodynamic efficiency. Furthermore, without the need for a pilot or cockpit, as this aircraft will be remotely piloted, we were able to optimize fuselage space for additional fuel and mission-critical equipment. This layout contributes to the efficiency and simplicity of the design by eliminating traditional cockpit infrastructure, allowing more

compact and modular systems.

Configuration decisions for the wing, empennage, and fuselage are detailed in Sections VIII.Aerodynamics, and VI.Interior Layout, respectively. In line with our design objectives, all major systems have been integrated to allow easy access and removal, facilitating operational maintenance and repair requirements. This modular, straightforward approach not only reduces costs but also supports faster deployment and turnaround times for essential equipment replacement. An overall isometric view from the top and bottom of the aircraft is shown in figure 8, showcasing the features of the aircraft, prominently the internal weapons bay as seen from the bottom with doors removed, revealing the missile load; note that the missiles are cylinders only intended to model the general geometry of the AIM-120.

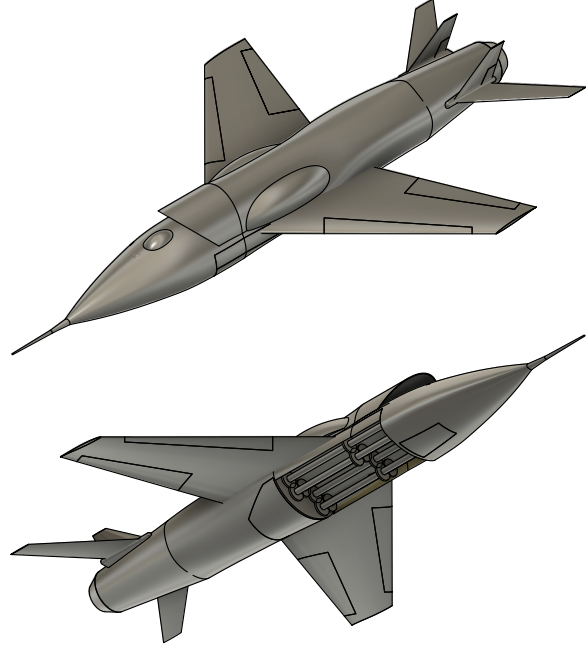


**Fig. 8 Aircraft configuration showcase**

## IV. Preliminary Sizing

This section outline the key steps in our approach to aircraft sizing, beginning with an initial weight estimate that considers mission fuel requirements, payload, and equipment, forming a foundation for further design refinements. Next, we present  $T/W$  vs.  $W/S$  plots to examine how thrust-to-weight and wing loading choices satisfy our mission and regulatory constraints, an improved weight estimate, and finally, we analyze a  $T$  vs.  $S$  plot, where cost objective function contours are overlaid to visualize the trade-offs in thrust and wing area for cost-effectiveness and mission performance. For more details on the computational methods and software implementation used to generate these plots, please refer to the Computational Procedure and Software Design section (XII).

### A. Initial Weight Estimate

Our initial weight estimation process was a key step in the preliminary sizing of the aircraft, allowing us to align potential design considerations with mission requirements and constraints. To begin, we broke down the mission profiles and analyzed each segment to estimate engine fuel consumption. Using historical data on fuel fraction estimates from Raymer [1], we calculated fuel needs for each mission segment, which revealed that the Defensive Counter-Air (DCA) mission required the most fuel, making it the primary driver in our weight estimation approach. Applying variations of the Breguet range equation along with historical fuel fraction values, we estimated fuel consumption for each segment relative to the previous one, creating a comprehensive profile of fuel requirements across all mission phases. These fuel estimates were then correlated with takeoff gross weight (TOGW) using historical data, providing a well-grounded basis for our initial weight figures.

Our design choice to operate the aircraft remotely allowed us to exclude weights associated with crew and life-support systems, focusing instead on camera and remote pilot equipment. Additionally, the weight of the six AIM-120 missiles and a fully loaded M61A1 cannon was factored into the payload, based on weights specified in the Request for Proposal (RFP). Together, these considerations helped us refine our weight estimate, ensuring the design was well-aligned with the operational requirements while keeping the overall weight as low as possible.

## B. T/W vs W/S

Our approach to generating the  $T/W$  vs.  $W/S$  plots was essential for selecting an optimal design point that met mission and operational constraints. First, we represented the operational requirements and mission phases as constraints, including takeoff and landing distances, flight ceiling, stall speed, maneuverability, climb capability, and excess power requirements.

For takeoff and landing, we used NATO's runway length standard of 8,000 ft, with equations 18, and 17 to calculate these constraints accurately. Climb requirements were based on meeting regulatory climb gradients, ensuring adequate operational performance in different mission phases. Maneuverability constraints were differentiated between instantaneous and sustained turns as specified in the RFP. For sustained turns, we selected a roll angle of 60 degrees (equivalent to a 2g load) which is typical for fighter jets [2]. The instantaneous turn was calculated from equations 19, 20, and 21, and the sustained turn was calculated from equations 22, 23, and 24. The rest of the constraint equations are highlighted in part D of the appendix.

By plotting all of these constraints together, we determined feasible regions within the  $T/W$  vs.  $W/S$  space, which guided our selection of a preliminary design point that was capable of meeting all requirements. The feasible region for max thrust is to the left of the landing field length constraint and above specific excess power at 1g, SL. For military thrust, it is to the left of the landing field length constraint, above specific excess power at 1g, SL, and above our takeoff climb.

From this  $T/W - W/S$  diagram, we selected a design point manually by observation, selecting the point with lowest  $T/W$  and highest  $W/S$  value within the feasible region. These plots and the selected design points are shown in Figures 9,10 and Table 4. An alternate figure with all constraints plotted together is shown in Figure 26 in the appendix.

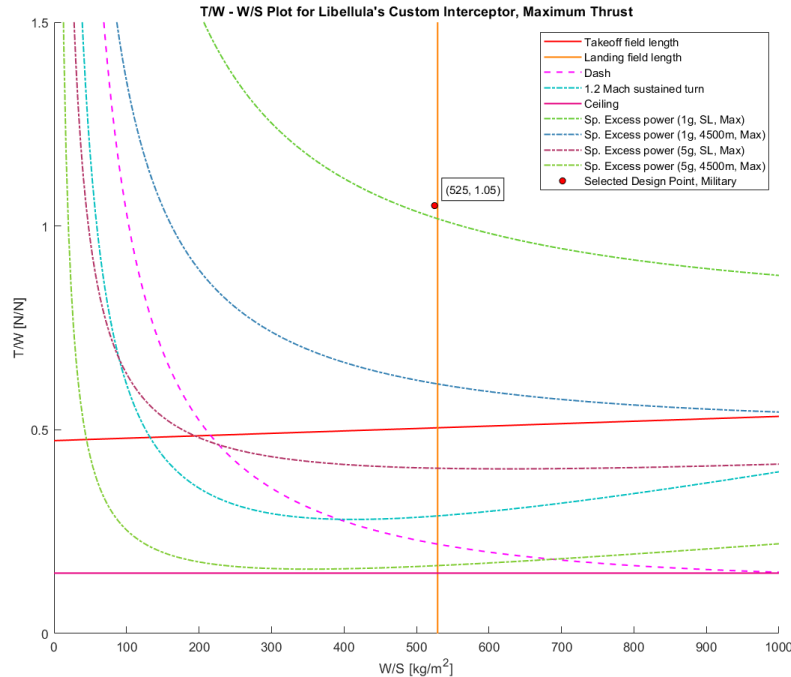


**Fig. 9**  $T/W - W/S$  Plot, Max Thrust

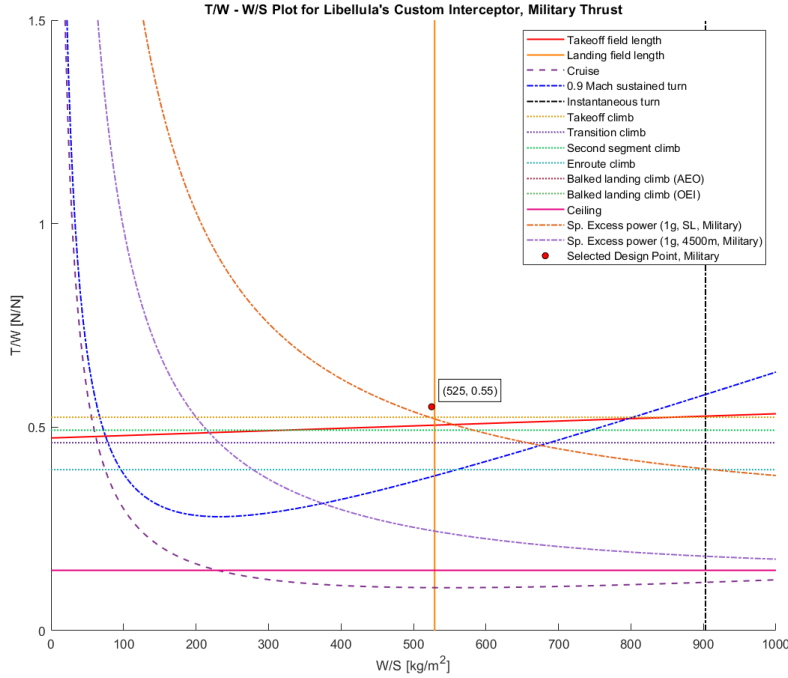


**Fig. 10 T/W – W/S Plot, Military Thrust**

Our selected design points are indicated on the graph, and repeated again in Table 4 for clarity:

**Table 4 Selected Design Points**

Parameter	Value
Wing Loading ( $W/S$ )	525 kg/m <sup>2</sup>
Maximum Thrust-to-Weight Ratio ( $T/W$ ) <sub>max</sub>	1.05
Military Thrust-to-Weight Ratio ( $T/W$ ) <sub>military</sub>	0.55

### C. Improved Weight Estimate

Our updated weight calculations provided a more accurate takeoff gross weight (TOGW) estimate by incorporating refined parameters based on the design points selected from our T/W vs. W/S plots. This updated process calculates empty weight using a regression model, where the design wing area and design thrust values are derived from TOGW and the selected design ratios. Adjustments to the empty weight account for specific input values of thrust ( $T$ ) and wing area ( $S$ ), applying area density adjustments and engine weight regressions from  $T$  to refine accuracy. With these updated empty weight values, we estimate a new fuel fraction based on wetted surface area and drag characteristics, incorporating them into the Breguet Range equation. The TOGW is iteratively refined through these steps until convergence is achieved, resulting in a more accurate weight estimate for the final design. Because this function also depends on  $T$  and  $S$ , we were able to plot cost contours (our objective function, discussed in section IX, which depends on TOGW) over our  $T - S$  diagram in order to select a point at minimum cost.

#### D. $T$ vs $S$ with objective function

Using the selected  $T/W$  and  $W/S$  design point along with our updated TOGW estimate function, we were able to plot the same constraints in the space of  $T$  and  $S$ , enabling us to select these key parameters for our aircraft design. Details on the computation of  $T$  and  $S$  from these inputs is discussed in section XII.

The space to the right of the landing field length line and above specific excess power at 1G, SL, for maximum thrust dictates our feasible region for  $T_{\max}$  and  $S$ . The space to the right of the landing field length line and above specific excess power at 1G, SL, for military thrust dictates our feasible region for  $T_{\text{military}}$  and  $S$ .

By overlaying cost contours over these constraints, we reached our final  $T$ - $S$  plot as shown in figure 11 and selected  $T_{\max}$ ,  $T_{\text{military}}$ , and  $S$  for our design. Cost was very sensitive with respect to  $T$ , and less so with  $S$  - confirming the dominant proportionality of thrust and aircraft cost. Identifying a point that minimized cost and gave some margin (which provides some flexibility if/when TOGW estimates increase), we selected  $24.5\text{m}^2$ ,  $76.3\text{kN}$ , and  $129\text{kN}$  for wing area, military, and maximum thrust, respectively. The yellow and orange dashed lines represent maximum and military thrust values, respectively for our selected engine (discussed in section X). An alternate figure with all of our  $T$  –  $S$  constraints as shown in figure 27. TOGW contours plotted over the constraining lines are shown in figure 28.

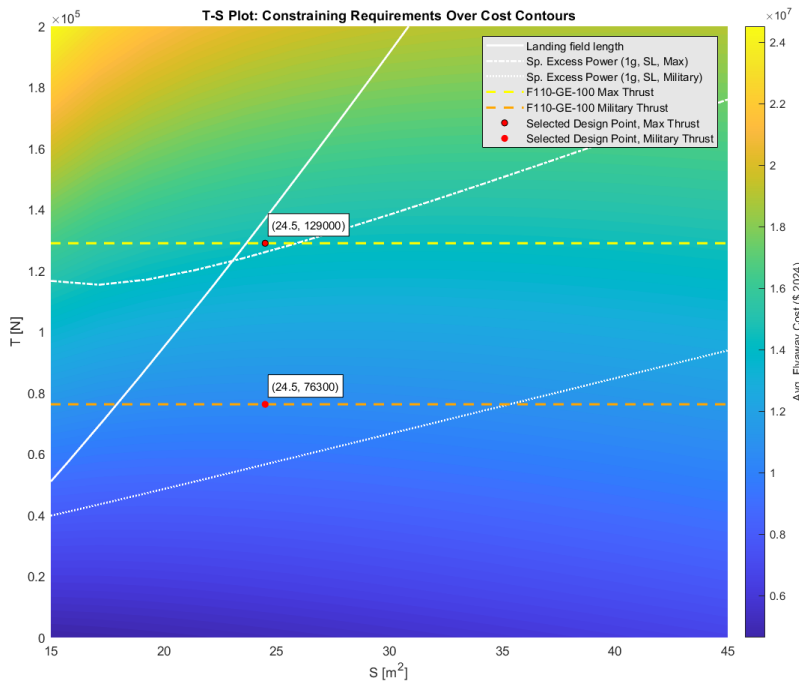


**Fig. 11**  $T$  –  $S$  Plot, constraining lines plotted over cost contours

To summarize, the final aircraft parameters decided from the  $T$  –  $S$  plot are listed in Table 7. The TOGW, empty weight, and DCA fuel fraction calculated from our updated functions for these selected  $T$  and  $S$  values are listed in Table 6.

**Table 5** Selected Aircraft Parameters

Parameter	Value
Maximum Thrust ( $T_{\max}$ )	129,000 N
Military Thrust ( $T_{\text{mil}}$ )	76,300 N
Wing Area ( $S$ )	24.5 m <sup>2</sup>

**Table 6 Updated Aircraft Weight Parameters**

Parameter	Value
Fuel Fraction (DCA Mission)	0.39
Empty Weight ( $W_e$ )	6300 kg
Takeoff Gross Weight ( $W_0$ )	12500 kg

## V. Interior Layout

### A. Interior Components

The fuselage interior was designed with an internal weapons bay and the additional constraints of increased fuel volume in mind; as such, the fuselage is relatively voluminous to accommodate for the fin diameters of the AMRAAMs as well as the fuel tanks. A previous iteration of our design featured area ruling around the fuselage midsection, which is almost totally masked by the addition of conformal fuel tanks above the wings. Even so, given the operability legacy of similar design configurations, including the more modern iterations of the F-16 or the F/A-18 which feature bulbous conformal fuel tanks, the design is not entirely unreasonable.

The high fuselage volume also allows for more space for cameras and observation devices for ground operators. Currently four different camera positions are proposed: the main "cockpit sight" camera located in the bulge ahead of the inlet, providing a 148° azimuthal view ahead of the aircraft; a secondary frontal camera ahead of the landing gear, providing a 110° azimuthal view below the aircraft; two rear cameras, above and below the fuselage, providing azimuthal angles of 133° and 121° respectively. View A in figure 12 shows the camera viewing angles. They were placed as to reduce the blind spots of the aircraft as much as possible. The cameras will be most useful in close quarter combat; in normal flight, and when engaging in BVR combat, the pilot will seldom need to look at any cameras other than the main camera, as the active array radar as well as the infrared search and track systems will serve as eyes to search for targets at long-range. In dogfights, the pilot will benefit most from a "stitched" array of monitors each displaying feed from each camera, which will enable the pilot to look around in a manner that will simulate an actual cockpit in the aircraft. This feature could be integrated with a helmet mounted display (HMD) to further enhance the capabilities of quick-response retaliation, but the associated cost could possibly be paramount. Even without this option, the IRST can provide effective target tracking over short distances.

View E in figure 12 outlines the offensive armament suite of our aircraft. The missiles are stowed in an internal weapons bay, shown open in figure 12, and is large enough to store six AIM-120 AMRAAMs. The cannon sits atop the weapons bay, along with its drum magazine, and fires out of a cannon port located to the right side near the termination of the nose cone.

The fuel tank locations were closely considered, and was the dominant component stored within the fuselage. View D shows an isolated view of the fuel tanks within the aircraft; fuel tanks were stored in the rear end of the nose cone (Nose fuel tank), around the cannon (cannon fuel tank), in bulges on the upper side of the fuselage (conformal fuel tanks), in both wings (wing fuel tanks), and below the engine (aft fuel tank). The center of gravity excursion as fuel and payload is depleted is described in the next section.

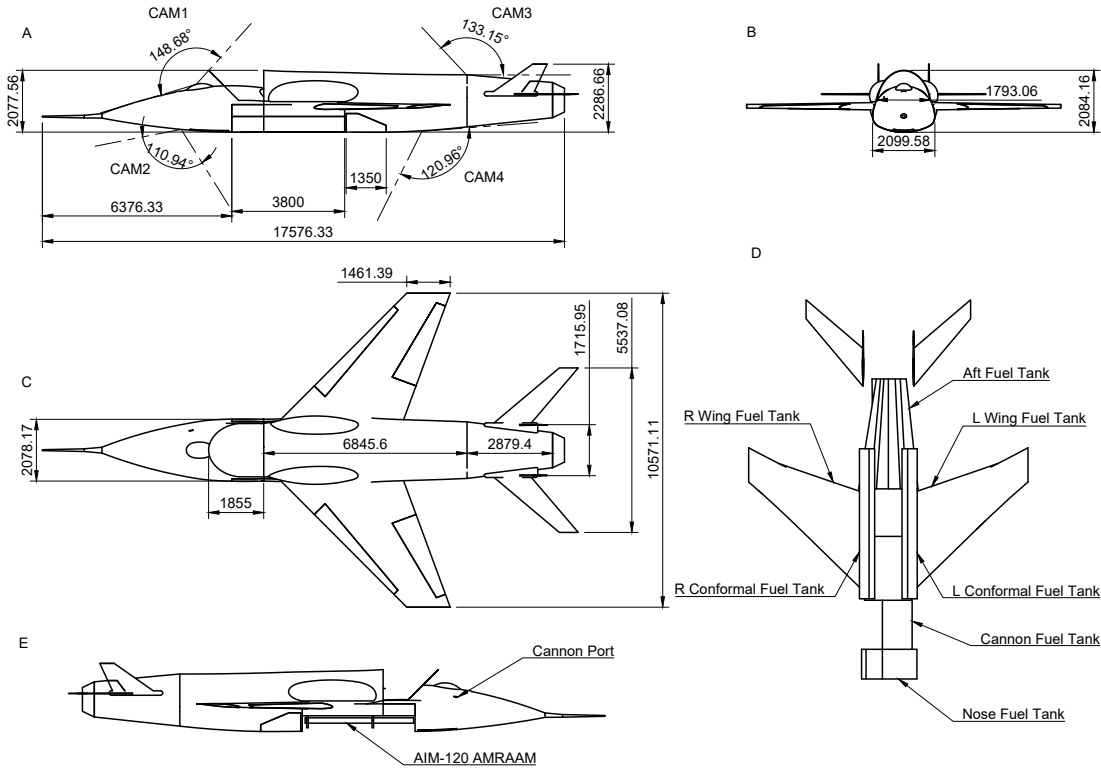


**Fig. 12 Aircraft interior breakdown with camera angles, fuel tanks, and payload**

### B. Component Weights and Aircraft Balance

Using the allocated positions of the internal components of the aircraft as described above, and using the weight values of Government Furnished Equipment (GFE) from the RFP, and considering fuel densities and volumes in each tank, a component-wise aircraft weight breakdown was developed. This allowed for a more refined analysis of aircraft balance. The weight breakdown is shown in figure 13.

The center of gravity was calculated using code that accepts the center of gravity locations and corresponding weights of each component of the aircraft and outputs the overall center of gravity of the complete aircraft. In particular, two states were of interest: the fully loaded state, which includes full fuel and weapons load, and the fully expended payload state, which removes missile and consumed fuel load from consideration. However, to better understand the progression of the movement of the center of gravity, the refueling and rearming process as well as the launching of each missile during flight was considered as separate "states" for consideration. Figure 14 shows the result of analysis of the movement of the center of gravity as a flight progresses.

Figure 14 indicates that the center of gravity begins at 10.87 m aft of the tip of the nose unfueled and unarmed, and moves continuously forward during the loading process to a final fully loaded center of gravity of 10.17 m. This poses no threat to aircraft tip-over on the ground as the main landing gear is projected to be located 11.78 m aft of the nose as seen in Figure 1, well behind the rearmost center of gravity. The effects of these changes in C.G. during flight will be discussed in the Stability and Control section.

## VI. Stability and Control

With a highly refined center of gravity estimation, stability analysis was made possible. A fundamental parameter in assessing the stability of the aircraft is the mean aerodynamic chord, which will be referred hereon as MAC. This is

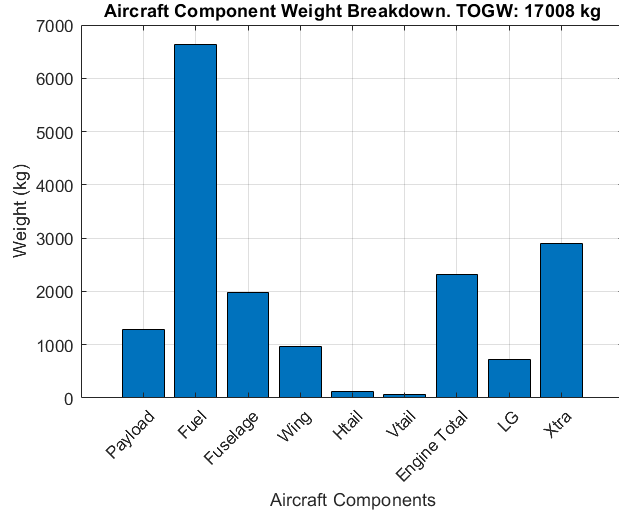


**Fig. 13 Weight Breakdown of Components**

defined as in Equation 1:

$$\bar{c} = \frac{1}{S} \int_{-\frac{b}{2}}^{\frac{b}{2}} c(y)^2 dy \quad (1)$$

The wing design, discussed in VII.A, yields a expression of the wing chord length as a linear function of the spanwise location. Evaluating the integral yields the chord length  $\bar{c}$ , and, using the inverse of the chord formula, the spanwise location  $\bar{Y}$  taken from the root of the wing. They are calculated as follows:

$$\begin{aligned}\bar{c} &= 3.045m \\ \bar{Y} &= 1.818m\end{aligned}$$

The MAC is crucial in determining the static margin of the aircraft and thus the neutral point; these parameters were derived from additional geometric parameters based on the CAD model. An approximation of the static margin, as outlined in *The Metabook of Aircraft Design*[3], is defined as follows:

$$-SM = \frac{x_{CG} - x_{np}}{\bar{c}} \approx \frac{x_{CG} - x_{25\%MAC}}{\bar{c}} + \frac{l_h S_h C_{L_{ah}}}{\bar{c} S_w C_{L_{aw}}} - \frac{\partial C_{m_{fus}}}{\partial C_L} \quad (2)$$

All parameters are immediately available from our integrated 3D model, except select variables;  $C_{L_{aw}}$ ,  $C_{L_{ah}}$  can be approximated with equations from the United States Air Force DATCOM [4] which are defined as:

$$C_{L_{aw}} \approx \frac{2\pi A R_w}{2 + \sqrt{(AR_w/\eta)^2(1 + \tan^2 \Lambda_h - M^2) + 4}} \quad (3)$$

$$C_{L_{ah}} \approx \frac{2\pi A R_h}{2 + \sqrt{(AR_h/\eta)^2(1 + \tan^2 \Lambda_h - M^2) + 4}} \left(1 - \frac{2C_{L_{aw}}}{\pi A R_w}\right) \eta_h \quad (4)$$

Where  $C_{L_{ah}}$  takes into account the downwash on the tail from the wake of the main wings. For these equations,  $\eta$  and  $\eta_h$  were taken to be 0.97 and 0.8 respectively, the latter being based on the evaluation that a tail higher than the main wing will be less efficient than a lower tail since it will be affected more by the wake in positive angles of attack. Additionally,  $\frac{\partial C_{m_{fus}}}{\partial C_L}$  was estimated based on an empirical formula developed by Robert R. Gilruth [5]:

$$\frac{\partial C_{m_{fus}}}{\partial C_L} \approx \frac{K_f w_f^2 L_w}{S_w \bar{c} C_L} \quad (5)$$

Where  $K_f$  describes an empirically derived coefficient relating the wing quarter chord position and its effect on the

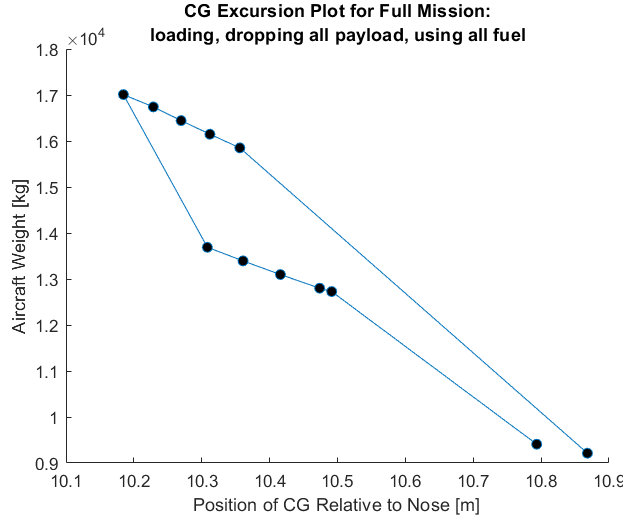


**Fig. 14 CG Excursion Plot for A Full Mission, Loading to Landing**

fuselage contribution on the static margin. This was estimated to be 0.718 for our aircraft. All other parameters are either known or derivable from the model, and two cases were considered for  $M$ : A cruise condition, and a takeoff/near stall condition, for which Mach numbers of 0.85 and 0.28 were used respectively; both were evaluated using a fully-loaded aircraft center of gravity. The resulting static margins and derived neutral points were calculated to be:

$$\begin{aligned} SM_{cruise} &\approx 0.04045, x_{np_{cruise}} \approx 10.310m \\ SM_{stall} &\approx 0.03120, x_{np_{stall}} \approx 10.280m \end{aligned}$$

Where the neutral points are stated relative to the tip of the nose. This is a weakly stable aircraft, which is favorable especially during takeoff where static stability is crucial in ensuring a successful takeoff. Considering the movement of the center of gravity as the mission progresses—which was described in the previous section—further calculations were made at differing stages of flight, as well as at different Mach numbers; it is shown in Figure 15 below that the static margin continuously decreases as the flight progresses, and eventually crosses into a region of moderate instability for all Mach numbers; the absolute minimum was observed in the case of a fully-expended aircraft at Mach 1.4, where  $SM = -0.1943$ . This instability will require a flight control system to effectively control the aircraft in the later stages of flight and landing. Figure 16 additionally provides information of how the neutral point changes as the flight Mach changes; it can be observed that the neutral point continuously shifts backwards until  $M = 1.0$ , beyond which the point travels forward again. This corresponds to an initial increase in SM for subsonic speeds then a decrease beyond Mach 1. Note that the dash Mach number of 1.6 is not included, as the approximating equations had no solution for large Mach numbers. According to the trend, we can reasonably infer that the dash phase will have a lower static margin, which reinforces the necessity of a FCS to effectively maintain stable flight in the dash phases of our missions. Refer to Figures 1 and 2 for geometric locations of relevant points along the length of the aircraft for the cruise conditions at full and fully expended states. A detailed design overview of control surfaces and empennage components is discussed in a later section.

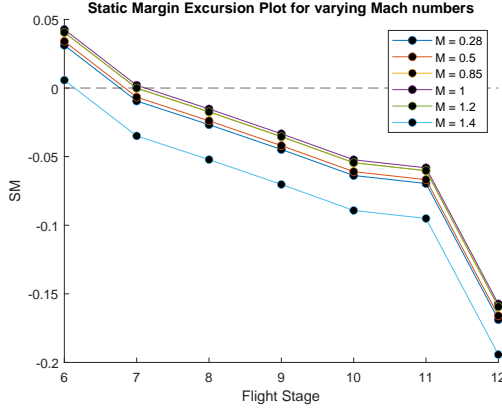


**Fig. 15 Static Margin excursion plot from takeoff to landing, at differing flight conditions**

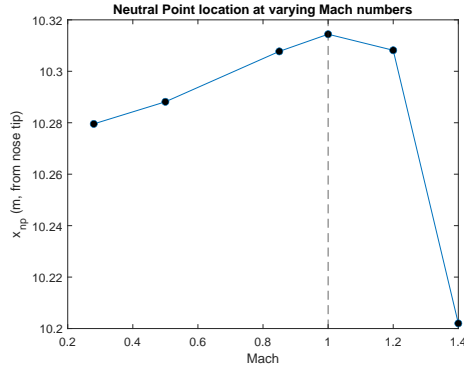


**Fig. 16 Neutral Point excursion plot with Mach number**

## VII. Aerodynamics

### A. Wing Design

This section discusses various assumptions and decisions related to the sizing of the wing of the aircraft. Our wing design balances maneuverability, efficiency, and structural integrity of our aircraft in order to meet the requirements of a Homeland Defense Interceptor.

#### 1. Wing Area

Our chosen wing area of  $24.5 \text{ m}^2$  was derived using our T-S plot (Figure 11) which identified our optimal thrust-to-weight and wing loading ratios based on our given constraints. Given a wing loading of  $528 \text{ kg/m}^2$ , the selected wing area supports the required lift across operation flight ranges for each mission.

#### 2. Aspect Ratio

A chosen Aspect Ratio of 3.068 was guided by trends in similar supersonic interceptors such as the F-16 Fighting Falcon [6] and the Lockheed F-104 Star-fighter [7]. We further investigated the advantages of a higher aspect ratio in order to reduce drag at low supersonic speeds and help delay the onset of shocks. We found that although, increasing the AR would consequently increase our maximum L/D, we did not want to make too substantial of a change that could decrease our stall angle of attack.

$$AR = 4.110 \times (1.6)^{-0.622} = 3.068 \quad (6)$$

We further refined our choice by utilizing Raymer's Method for calculating equivalent aspect ratios [1] shown in Figure 18. This derivation based on historical data allowed us to choose an AR that minimizes drag by delaying shock formations while preserving lift at higher angles of attack and ensures efficiency at Mach 1.6 with minimal impact on the stall angle.

Jet Aircraft	Equivalent Aspect Ratio = $aM_{\max}^C$	
	$a$	$C$
Jet trainer	4.737	-0.979
Jet fighter (dogfighter)	5.416	-0.622
Jet fighter (other)	4.110	-0.622
Military cargo/bomber	5.570	-1.075
Jet transport	7.50 to 10	0

**Fig. 17** Raymer's Method for Calculating Fighter Jet Aspect Ratios

### 3. Span

The Span is later derived consequently from these two parameters using the relation that span length,

$$b = \sqrt{AR \times Sref} = 8.67m \quad (7)$$

### 4. Taper Ratio

Taper Ratio is defined as the ratio of tip chord to the root chord. For supersonic interceptors, using a moderately lower taper can result in reduced wing weight which is beneficial for our high speed segments. We chose a taper of 0.35 because this particular ratio improves our span-wise lift distribution and reduces the induced drag associated with high speeds. Also compared to similar supersonic aircraft, the taper ratio should range between 0.30 - 0.40 for a balance of high speed stability and structural integrity [8].

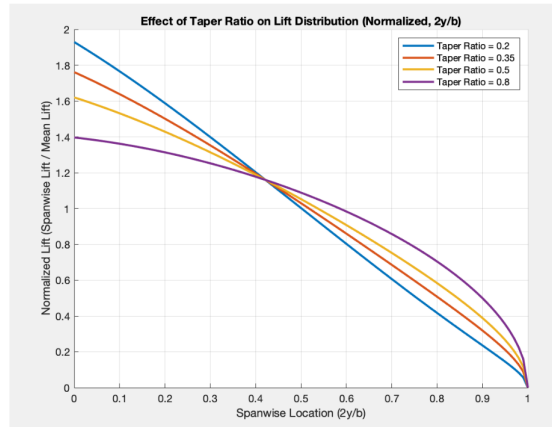


**Fig. 18** Normalized Lift Distribution for Various Taper Ratio

### 5. Wing Incidence And Twist

For fighter jets, a typical root incident angle is between  $1^\circ$  to  $2^\circ$ , which helps optimize our lift to drag ratio during high speed cruise, particularly in the supersonic segment. Our chosen low incident angle of 2 degrees reduces drag, which is essential for our design [9].

The twist or washout for a supersonic aircraft based on historical data ranges between  $-1^{\circ}$  to  $-3^{\circ}$ . For our chosen taper of 0.35, a  $-2^{\circ}$  twist was chosen to ensure that the wing tips have a lower angle of attack compared to the root. This will prevent tip stalling during low speeds segments of the mission such as takeoff and landing where the aircraft is more prone to instability. A small amount of twist will help us achieve more optimal lift and be closer to an elliptical lift distribution[10].

## 6. Sweep

The sweep angle is critical for our performance parameters because it aids in reducing drag considerable during supersonic speeds. Especially at transonic speeds—which we are hoping to optimize for—the wing sweep will mitigate the adverse drag from transonic flow and increase the speed at which shocks will begin to form. Introducing sweep will also increase our aircraft's lateral stability given our speed requirements and maneuverability constraints.

We began our derivation of sweep by utilizing a method established by Raymer [1] that allows us to estimate our quarter chord sweep from our determined aspect ratio, shown in Figure 19. This led us to choose a quarter chord sweep around 40 degrees from the transonic flight region.

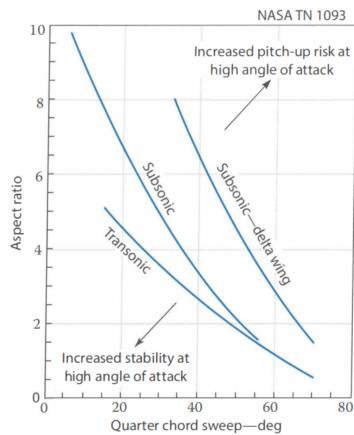


**Fig. 19 Determining the Quarter Chord Sweep from our Aspect Ratio**

We then determined the leading edge sweep according to the following equation [1]:

$$\tan(\Lambda_{LE}) = \tan(\Lambda_{c/4}) + \frac{1 + \lambda}{AR \times (1 + \lambda)} \quad (8)$$

Where our aspect ratio ( $AR$ ) is defined as 3.068, the taper ratio ( $\lambda$ ) is equal to 0.35, and the quarter-chord sweep ( $\Lambda_{LE}$ ) is 35 degrees. This would then yield a leading edge sweep value of around 45 degrees. We later verified our assumptions

by ensuring that at this specific leading edge sweep, our wing remains supersonic up to a speed of Mach 1.2, which is the speed we would see in combat. This was derived from the component break down of the speed at the leading edge of the wing. We ensured that at the critical Mach number our wing remained behind the mach cone in order to prevent supersonic flow over the wing and causing wave drag [11]. After refinement, we established our leading edge sweep to be 44.9 degrees.

We also derived our Critical Mach number to be 0.85, which based on historical data collected in Raymer and based on the thickness ratio of our selected airfoil. Figure 20 shows our selection method [1].

## 7. Wing Configuration

Our wing will be placed in a mid-wing configuration. This allows the wing to be streamlined with the fuselage to minimize interference drag at transonic speeds. This will also enhance performance of high G turns and rapid

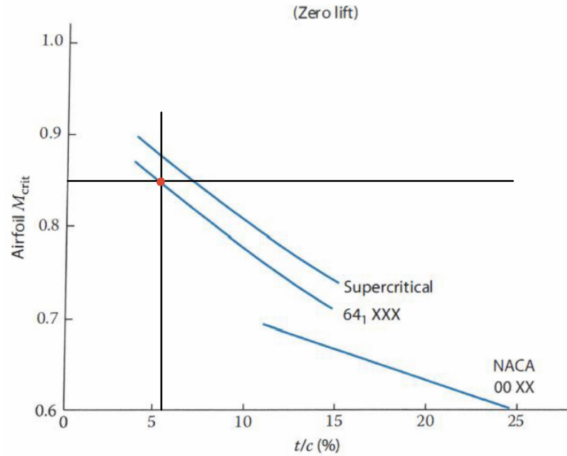


**Fig. 20 Critical Mach number as a function of Thickness Ratio**

maneuvers. Mid wings avoid ground clearance issues associated with low-wing designs and the over-stability in roll associated with high-wing configurations. Mid wings are most aligned with the center of gravity of the aircraft and reduce roll inertia [12].

Our wings will also be cantilevered. Braced wings produced far too much drag at high speeds to be feasible for the mission requirements we are tasked with. Our aircraft will also have a dihedral angle of  $0^\circ$ . We designed our aircraft with neutral stability in mind and want to ensure our aircraft can quickly adapt to changing flight conditions as well as maintain sufficient control during cruise and combat. Overall, these design parameters within the wing configuration allow for simpler and more cost-effective structural reinforcements, which aligns with our primary objective function to maintain low cost while ensuring responsive control [12].

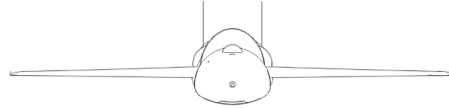


**Fig. 21 CAD Image of Our Aircraft's Wing Configuration**

### 8. High Lift Devices

**Leading edge extensions/stakes** are still under refinement as we have not yet incorporated them into our 3D CAD model. However, we plan to integrate them into our aircraft design. These extensions are critical for combat effectiveness, as they increase the stall angle of attack and lift by generating lift-inducing vortices over the wing. This feature enhances the interceptor's performance, especially in high-angle maneuvers, elevating its overall combat capability [13]. These leading edge extensions also help deal with the isobar unsweep problem at the root of the wing [1]. Incorporating a leading edge extension, however, can promote pitch-up tendencies so this is one drawback we will need to consider when finalizing the stability of our aircraft.

In our design, we've opted to use **flaperons**, combining flaps and ailerons into a single control surface. This integration offers significant advantages in terms of both cost and performance, simplifying the wing structure and reducing overall aircraft weight. The combined flaperon design provides the remote pilot with more precise control authority by unifying roll and lift management into one system. This control surface setup is also essential to counteract

the reduced lift associated with our thin airfoil, ensuring adequate lift during takeoff and landing [13].

The flaperon sizing was based on guidelines from Raymer's textbook [1], with parameters including an aileron-to-wing chord ratio of 0.35—a ratio supported by historical data limits—a span ratio of approximately 0.6, since flaps positioned closer to the wing root generate higher lift forces, and a taper ratio of 0.75 to minimize additional wing weight, which enhances stability. The equations and historical data used for these specific sizing parameters can be found in the Appendix, Figure 31

We will incorporate the use of **leading edge flaps** to effectively increase the camber of the airfoil, enhancing lift during high angle of attack maneuvers and supporting additional lift during low-speed phases such as takeoff and landing. These flaps offer a straightforward design that helps reduce weight and cost, making them easier to integrate into the aircraft's dynamic control system for combat scenarios. Unlike slats, leading edge flaps maintain a seamless airfoil shape that supports high-performance maneuvers without the increased drag that can result from slat gaps.

## B. Airfoil Selection

The wings of our aircraft are designed around the NACA 64A-206 airfoil. This decision was based on historical data of similar aircraft, such as the F-16, which we share similarities with regarding empty weight and wing loading [6]. In the F-16, and other training jets, the NACA 64A-206 airfoil is a considerable option during flight because these aircraft have the ability to change the geometry of the wing by deflecting the leading or trailing edge flaps. This effective change in the camber and curvature of the airfoil allows for resulting changes in lift, drag, and pressure coefficients. Although we are incorporating similar trade-offs for our control surfaces, our airfoil choice is subjected to change due to concerns regarding its ability to perform efficiently during supersonic flight.

The NACA 64A-206 airfoil is not considered a supercritical airfoil and is a rather older design that could prevent us from fulfilling our requirements outlined in the RFP. Due to these discrepancies, we have decided to consider two additional airfoils that could be incorporated to our wing design.

First, we are considering the TsAGI S-12 airfoil. This airfoil is suitable for high-speed, supersonic applications that require stability and agility in combat. The TsAGI S-12 was designed specifically with high-speed, maneuverable aircrafts in mind and will help us address the critical needs for our interceptor to operate at speeds up to Mach 1.6.

The TsAGI S-12 airfoil's shape minimizes drag at supersonic speeds by having a sharp leading edge and a lower thickness-chord ratio, which is particularly important as the aircraft transitions through the transonic and supersonic regimes. The thickness-chord ratio is around twelve which is higher than the other two airfoils we are considering so that factor will weigh into our decision of airfoil selection. However, this airfoil was applied in aircraft like the Mikoyan-Gurevich (MiG)-21, a supersonic interceptor with similar performance needs and allowed for overall efficient high-speed flight with reduced drag penalties [14].

We are also considering the NASA SC(2)-0614 airfoil. The SC(2)-0614 has a 6% thickness-to-chord ratio, making it thinner than many traditional airfoils and better suited to minimize wave drag in supersonic flight. The sharp leading edge is optimized to create weaker oblique shocks, which helps in maintaining smoother airflow across the surface at high speed. In combat scenarios, where agility and lift control are crucial, the SC(2)-0614 provides stability at high angles of attack while preserving lift [15].

These two airfoils are still being considered in order to address the concern surrounding our current airfoil; however, further refinement will be made in later assignments throughout the coming weeks in order to prepare for our critical design review. The corresponding drag polar of each airfoil can be found in Figure ?? in the Appendix.

### C. Stall Speed

To calculate the stall speed of the aircraft, we utilized a method following the design process of past aircraft. With the relation provided in equation 9 [1], we can input parameters from our aircraft to yield an estimate of the velocity we will experience stall at. With a  $C_{L,max}$  of 1.25 in the aircraft's clean configuration, a  $W_0$  of 12,500 kg multiplied by  $g = 9.81 \text{ m/s}^2$  (provided that takeoff weight will yield the most critical case),  $S_{ref}$  of 24.5 m, and  $\rho$  of  $1.225 \frac{\text{kg}}{\text{m}^3}$  at sea-level, we attained a stall speed velocity of 80.85 m/s. We believe that this is a reasonable stall speed for our aircraft, as most fighter aircraft have a stall speed ranging from approximately 70-110 m/s.

$$V_{stall} = \sqrt{\left(\frac{2}{\rho \times C_{L,max}}\right) \times \left(\frac{W_0}{S_{ref}}\right)} \quad (9)$$

### D. Empennage Configuration

#### 1. Vertical Tail

Our inlet design choice, top speed, cost considerations and preliminary analysis of our lifting surfaces determined the configuration of our vertical tail. We selected a top-mounted engine intake which requires that we separate the vertical tail and its control surfaces from the wake that will be produced during level, maneuvering, and high A.O.A. flight. The less turbulent flow surrounding and interacting with the vertical tail, the higher the retention of the aircraft's control authority. We achieve this by separating our vertical stabilizer into a vertical twin-tail configuration. Another benefit of a twin-tail configuration is that it allows the aircraft to isolate yaw actuation, which simplifies the aircraft's dynamics and could reduce the amount of time spent in flight tests, thus saving development costs.

The vertical tail was swept by  $\Lambda = 55^\circ$  following historical data from Raymer [1]. This number was verified by identifying a chord-wise Mach number of 0.918 at our maximum speed of  $M = 1.6$  using equation 10.

$$M_{chord} = M_{freestream} \cos(\Lambda_{VT}) \quad (10)$$

This shows that our airfoil will largely see transonic speeds during the dash phase. Transonic flow allows us to delay shockwave formation and reduce wave drag while also trending toward a high enough Mach number at our maximum thickness to chord point ( $\approx 0.5c$ ). This will help maintain subsonic flow onto the rudder, which begins at  $0.7c$  and extends to the trailing edge. An aspect ratio of  $AR = 2$  was selected to reduce the induced drag affecting the rudder, which will be placed at the vertical tail's root. This value is on the higher end for fighters according to Raymer Table 9.3 [1].

Raymer Table 6.5 [1] shows that fighter jet rudders typically extend to 30% of the vertical tail's span. Our design proceeded with the assumption that this value can be used for both single and dual tail configurations given that the same total lift must be produced to control the aircraft. A preliminary lift distribution analysis was conducted with the same methodology used in section VII.A.4 for the wing taper. We selected a taper of  $\lambda = 0.35$  given that its high value will help reduce induced drag. This led us to choose to extend our rudder span to 38% of the tail to capture  $\approx 50\%$  of the lift produced by the tail as seen in Figure 22.

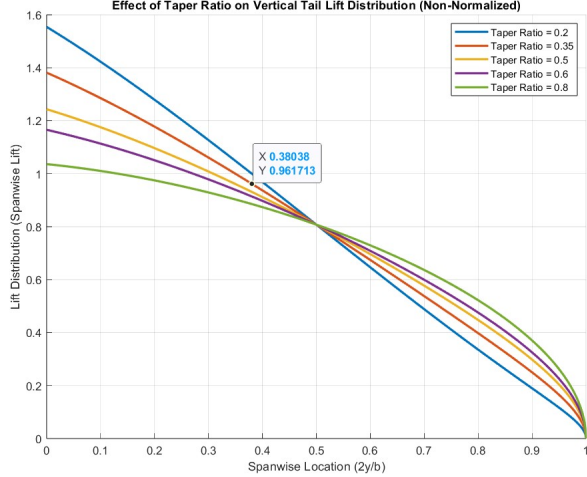


**Fig. 22 Non-Normalized Lift Distribution on Vertical Tail with Varying Taper Ratios**

In the near future this extension may have to be lowered to the historical value or extended to the full tail span (like in the Kratos XQ-58 Valkyrie UAV). This would be necessary if CFD analysis shows the interactions between the vortices formed by the tail tip and upper edge of the actuated rudder to have significant negative effects on the flow over the platform.

## 2. Horizontal Tail

As mentioned in section VI, our aircraft will be stable during takeoff (low speed) and unstable during cruise (transonic speeds) and dash (supersonic speeds). This requires an all-moving horizontal stabilizer with control authority at all speeds and therefore very careful airfoil selection and design, which will be expanded on in section VII.E.

The horizontal tail's sweep and placement were determined to ensure that it stalls after the wing. This included sweeping the leading edge by  $5^\circ$  or  $\approx 11\%$  more than the leading edge of the wing, resulting in a final sweep of  $\Lambda = 49.5$ . This was done because a lower chord-wise Mach number will reduce the probability of flow separation. The horizontal tail's placement was guided by a chart built from an experimental study conducted by NACA [16] that guides a tail's vertical placement ( $\frac{\Delta z}{c}$ ) with respect to the x-z coordinates of the wing's M.A.C. depending on  $\frac{x_{tailarm}}{c}$ . This value was calculated using the following equation 11.

$$\frac{x_{tailarm}}{c} = \frac{x_{MAC_{wing}} - x_{MAC_{tail}}}{c} \quad (11)$$

A margin of approximately  $-0.1(\frac{\Delta z}{c})$  was added to the minimum allowable vertical distance. This resulted in  $\frac{\Delta z}{c} = -0.2$ ,  $\Delta z = -0.6096m$  after a careful visual inspection of Figure 3 in [16].

We aim to have a lift-efficient horizontal stabilizer due to the low lift that thin airfoils produce at takeoff. This led to an aspect ratio selection of  $AR = 4$ , which remains within the bounds of historical values listed in Raymer Table 6.4 [1]. Our taper ratio analysis showed that a value of  $\lambda = 0.5$  would get us fairly close to an elliptical lift distribution while still allowing us to utilize our high aspect ratio. The following lift distribution may be found in the appendix as Figure 37.

Our airfoil selection and consequent analysis of  $\frac{\partial C_{L_h}}{\partial \alpha}$  shown in section VII.E will provide more clarity on the horizontal stabilizer's effect on longitudinal stability.

## E. Airfoil Selection

### 1. Vertical Tail

A biconvex airfoil with a 3.3% thickness to chord ratio was selected due to its sharp leading edge and gradual increase in thickness along its chord. The sharp leading edge will allow optimal performance at supersonic speeds given that it will generate an oblique shock that will slow down the flow coming onto the rudder. This airfoil provides a nice balance between shock delay and allowing space for subsonic flow into our control surfaces when assuming that in the transonic regime the shock will form at the maximum  $\frac{l}{c}$  location (0.5c for a biconvex airfoil). The vertical tail sweep will be determined with the aim of having the leading edge see a speed of no less than  $M = 1$ . If we rearrange eq. 10 to solve for sweep angle we can find that the sweep will have to be redesigned and set to  $\Lambda \approx 51.31$  for CDR. However, this value will have to be verified with CFD analysis.

### 2. Horizontal Tail

The horizontal tail airfoil poses an interesting challenge given that it must produce sufficient lift to rotate during takeoff, provide a controlling force at both positive and negative incidence angles -given our transition from stable to unstable during flight- and minimize wave drag. These considerations lead to design constraints such as symmetry, and low  $\frac{l}{c}$ . While the biconvex airfoil has both the symmetry that our aircraft's varying stability requires, low  $\frac{l}{c}$  and the gradual thickness increases that will allow for a gradual shock development along its chord it has terrible lift production at low speeds. Viscous vortex panel simulations were unsuccessfully attempted on this airfoil, given that these simulators are meant to be used on airfoils with rounded leading edges. Hence, a lift curve slope analysis was performed on NACA 0003 as a very rough estimate for the properties of an airfoil of similar thickness and symmetry. For the moment, the design will maintain the biconvex airfoil until we learn how to design a custom hybrid airfoil before CDR. However, our preliminary estimates of what will be necessary for this airfoil include a slight forward movement of the max thickness and a rounded leading edge small enough to form an oblique shock but large enough to produce suction peak-like behavior at subsonic speeds.

When it comes to this airfoil's effects on our longitudinal stability, the simulations for NACA 0003 were used to obtain a lift curve slope at take-off and cruise. Results can be seen in Figures 38 and 39. Results from a research paper [17] characterizing a biconvex airfoil at multiple supersonic Mach numbers were used to estimate the lift curve slope in this regime. The results were analyzed for the match number most similar to what the horizontal tail will see ( $M = 1$ ), and a regression was performed with data points from the segment where the lift curve slope behavior is closest to a linear relationship. Results may be seen in Figures 41 and 40. These values were then multiplied by the downwash correction factor in eq. 4 and are visible in 17.

## F. Dimensions After Volume Coefficient Based Sizing and Airfoil Selection

Volume coefficients were taken from historical values in Raymer Table 6.4 [1]. Consequently, our horizontal tail volume coefficient  $c_{HT} = 0.4$  and our vertical tail volume coefficient came out to  $c_{VT} = 0.07$ . This allowed us to solve for both tails' platform areas and obtain our geometric parameters by following the same sizing process as the wing.

These parameters are listed in Table 17 in the appendix (section XV).

## VIII. Method Validation

To validate our software, we populated our aircraft struct with parameters that describe the F-35. All values were pulled from the student guide [18]. Most significantly, we defined the crew weight, payload weight, wing loading, and thrust to weight ratio of the F-35, as these are the key values our software uses to calculate the maximum TOGW (MTOW) of the aircraft.

Subsequently, we ran an iteration on our `togw_as_func_of_T_S_calc.m` function, which calculates the maximum TOGW of an aircraft given an input wing area and maximum thrust. The input values for this validation are as follows:

**Table 7 F-35 Parameters for TOGW Calculation**

Parameter	Value
Maximum Thrust, $T$ (N)	190,000
Wing Area, $S$ ( $\text{m}^2$ )	42.7
Maximum Takeoff Weight, MTOW (kg)	29,900
Max Thrust-to-Weight Ratio, $T/W$	0.65
Wing Loading, $W/S$ ( $\text{kg}/\text{m}^2$ )	700

In validating this function, we made one additional key modification. Our software calculates the fuel fraction of the designed aircraft based on the DCA mission provided in the RFP, which is a much more demanding mission with respect to range than the F-35's mission. Consequently, we fixed the fuel fraction in the `togw_as_func_of_T_S_calc.m` iteration to 0.28, which is the F-35's fuel mass, 8,300 kg (18,250 lbm) divided by its MTOW. Consequently, we are not validating our fuel fraction function. This is acceptable, as its calculation is specific to our mission alone.

Running our function with these inputs and modifications yields:

**Table 8 TOGW Function Validation Summary**

Actual Weight (kg)	Calculated Weight (kg)	Percent Difference (%)
29,900	31,900	6.69

We deem our percent error, 6.69%, to be sufficiently low for our preliminary weight estimations. When plotting the F-35 design points on our  $T/W - W/S$  and  $T - S$  plots, the point does not fall within our feasible region. This is expected, as the F-35 does not have the same constraints that our aircraft does. These constraints are not readily available online, but can be roughly solved for given the F-35's specifications. Time permitting, we will pursue this validation of our constraint diagrams in CDR.

## IX. Objective Function

As outlined in the RFP, this interceptor will address the need for an affordable aircraft within the US Air Force and Navy fleets. The F-35 and F-22, designed for air superiority, are too costly to be procured in the quantities required to

strengthen US defense amid rising international political tensions. Consequently, our aircraft should be as inexpensive as possible while meeting all other operational capabilities, and have defined cost as our objective function.

We utilize method A13 in Roskam's Airplane Design [19] Section 8, Appendix A for calculating the flyaway cost of a military aircraft as a function of TOGW:

$$\text{cost}_{1989} = 10^{2.3341 + 1.0586 \cdot \log_{10}(\text{Wto})} \quad (12)$$

This gives us a rough estimate of the flyaway cost in 1989. Adjusting for inflation:

$$b_{\text{CEF}} = 5.17053 + 0.104981 \cdot (1989 - 2006) \quad (\text{Base year CEF}) \quad (13)$$

$$t_{\text{CEF}} = 5.17053 + 0.104981 \cdot (2024 - 2006) \quad (\text{Target year CEF}) \quad (14)$$

$$\text{cost}_{2024} = \text{cost}_{1989} \cdot \frac{t_{\text{CEF}}}{b_{\text{CEF}}} \quad (\text{Adjusted cost}) \quad (15)$$

Lastly, we adjust the flyaway cost for our aircraft based on a 95% learning curve, which allows us to project cost savings associated with the efficiency gained with increased production. We chose a 95% learning curve as a conservative estimate - with newer manufacturing technologies such as additive manufacturing and CNC, the improvement seen over time will be diminished, but not zero.

$$\text{cost}_{2024,\text{adj.}} = \text{cost}_{2024} \cdot \left( \frac{1}{Q_i} \right)^{1-x} \quad (16)$$

is the formula taken from Raymer 18.4.1 [1],  $x = 0.926$  for a 95% learning curve,  $Q$  is the number of aircraft being produced, and  $\text{cost}_{2024,\text{adj.}}$  is the unit flyaway cost of the  $Q^{\text{th}}$  aircraft produced. To find the average cost of an aircraft for a given  $Q$ , the mean was calculated over the unit costs for  $Q_i = 1$  to  $Q_i = Q$ . The contours of this objective function (with  $Q = 1000$ , as defined in the RFP) were plotted on the  $T - S$  graph and used to select the design point.

Given our estimated TOGW of 12,500 kg, the average cost for the first  $Q$  aircraft was:

**Table 9 Average Flyaway Cost by Quantity Produced**

$Q$	Avg. Flyaway Cost
250	\$16.1 M
500	\$15.3 M
1000	\$14.6 M

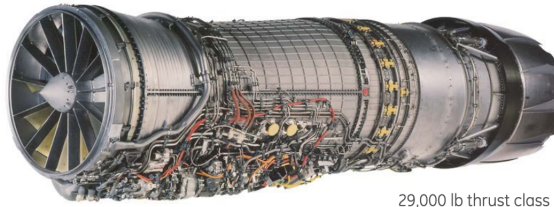
Because our initial estimates provide values lower than the RFP constraint of \$25 million in all three cases, we are confident that our approach is aligned with our requirements. We will calculate a more accurate estimate of flyaway cost for CDR that calculates cost by a component breakdown with DOC and IOC, including factors such as manufacturing,

maintenance, R&D, and fuel.

## X. Propulsion System

The engine selected for our aircraft is the F110-GE-129 (shown in Figure 23). This provides 129kN of thrust at MAX throttle and 76.3kN at MIL throttle, matching the thrust requirements discussed in the sizing section above. With a legacy of being applied on the F-15E and later versions of the F-16, the engine was deemed to be the best choice in terms of value and performance. A dual engine configuration necessitated a larger cross-sectional area of the fuselage especially towards the rear of the aircraft and a larger flow rate which would also inevitably contribute to the general size of the aircraft. Even if a single engine configuration puts our aircraft significantly below the thrust levels of 4+ to 5th generation fighters currently in service today, our high T/W ratio as well as the maneuverability considerations will help our aircraft be competitive in combat.

The engine inlet was designed to sit on the top of the fuselage. This is highly unconventional for a frontline military aircraft, but may prove to be a versatile design. The lack of a pilot facilitates the feasibility of such a design, and the shock-inducing hump (which serves another purpose of housing the main frontal camera) helps create a positive pressure gradient immediately downstream that diverts low-energy boundary layer flow to either side of the fuselage as reported by Ge et al [20], ensuring clean airflow delivery. Another concern for a top-mounted inlet is performance in high AoA, where the inlet may see less airflow or even have a risk of stalling. The inlet, at high angles of attack, being near the nose of the aircraft, will see air swept around the bubble-shaped nose from the high-pressure lower side to the upper, inducing a vortex pair that serve to re-energize the flow and provide some margin from critical airflow even in extreme conditions as observed by Tan and Guo [21]. Additionally, iterations were made in the duct traveling towards the engine inlet plane that initially resembled an S-duct, but was moderately straightened in the current iteration to maximize pressure recovery and minimize distortion associated with curved ducts.



29,000 lb thrust class

Fig. 23 F110-GE-129 Engine Selection

## XI. Government Furnished Equipment

As outlined in the Homeland Defense Interceptor RFP, Government Furnished Equipment (GFE) was used to the furthest extent. A list of all GFE available and our rationale is shown in the following list and in Table 10:

- 1) **Integrated Communication, Navigation, and Identification Avionics:** Included; fundamental avionics equipment necessary especially as an uncrewed aircraft.
- 2) **Multifunctional Displays:** Not included; MFDs not needed onboard in the absence of a pilot.
- 3) **Head-Up Display:** Not included; HUDs not needed onboard in the absence of a pilot.
- 4) **Data Bus:** Included; effective aircraft data and telemetry handling is crucial for an unmanned system.
- 5) **Integrated Electronic Warfare System:** Included; in the event of retaliation by intercepted enemy aircraft, effective deterrence and defensive countermeasures are not only desired, but also necessary.
- 6) **Vehicle Management System:** Included; aircraft health is much more difficult to assess as a ground operator;

the VMS can handle and deliver such crucial information to the operator.

- 7) **Infra-Red Search and Track System:** Included; a passive method of target tracking, even in the absence of heat-seeking infrared guided missiles to complement, can greatly contribute to surprising enemy aircraft.
- 8) **Active Array Radar:** Included; fundamental avionics needed to track targets at long range and lock targets for AMRAAMs.
- 9) **Engine Electrical System:** Included; FADEC control and related electrical subsystems critical to effective engine control.
- 10) **Auxiliary Power Unit:** Included; APU needed for startup or emergency engine restart during flight.
- 11) **Onboard Oxygen Generation System:** Not included; not needed onboard in the absence of a pilot.
- 12) **Onboard Inert Gas Generation System:** Not included; although higher fuel volume increases risk of fires, ultimately serves to take up more space to reach all fuel tanks around the aircraft. An alternative solution of using self-sealing fuel tanks should be pursued.
- 13) **AIM-120 AMRAAM:** Included; part of the basic weapons load, effective in beyond visual range (BVR) combat.
- 14) **M61A1 Cannon:** Included; part of the basic weapons load, more useful in extremely close-quarters combat.

Figure 24 below shows the interior of the aircraft in top and side views, highlighting all GFE integrated in the system. We have yet to make a selection for a specific camera/vision configuration that would enable remote piloting, and will do so moving forward with CDR.

**Table 10 GFE Table**

	Equipment	Quantity	Volume [ft <sup>3</sup> ]	Weight [lbs]	Cost [USD]
Avionics	ICNIA	1	3.0	100	200K
	Data Bus	1	0.5	10	10K
	INEWS	1	3.0	100	500K
Flight & Propulsion Control System	Vehicle Management System	1	1.0	50	200K
Fire Control Systems	IRSTS	1	2.0	50	200K
	Active Array Radar	1	6.0	450	1000K
Systems & Equipment	Electrical System (for 1 engine)	1	3.0	220	42K
	Auxiliary Power Unit	1	2.0	100	50K
Air-to-Air Weapons	AIM-120 AMRAAM	6	20.4	1962	2316K
	M61A1 20mm Cannon	1	10.465	575	250.29K
Total				3617	4768.3K

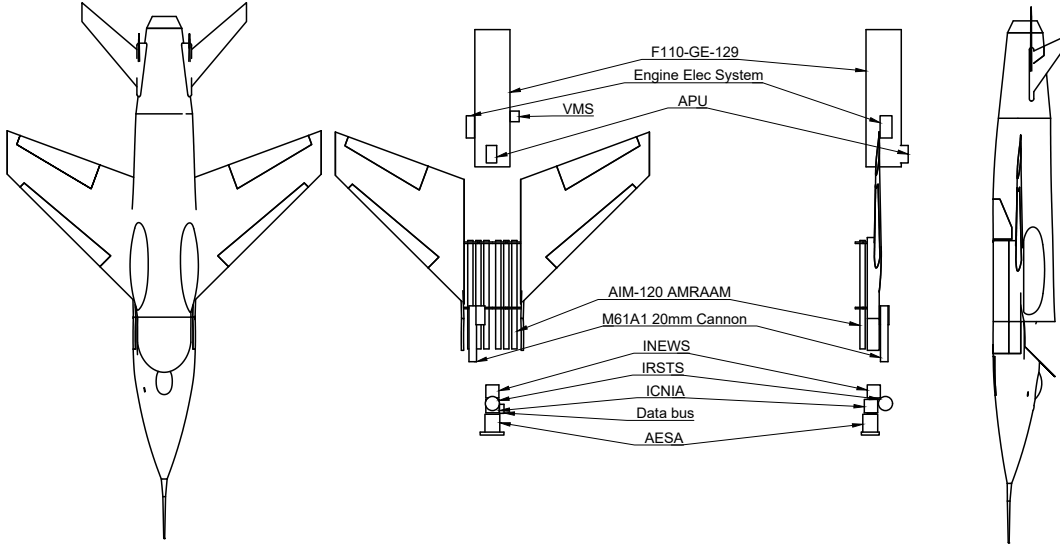


**Fig. 24 GFE locations within the aircraft in top and side views**

## XII. Computational Procedure and Software Design

To assist us in defining design constraints, selecting a design, and optimizing it, we built a comprehensive aircraft sizing software package from the ground up, incorporating methods from Martins [3], Raymer [1], Roskam [19], and other aircraft designers. Our software is implemented entirely in MATLAB due to its compatibility with large, complex, nested data structures and the familiarity of our team with the platform.

Significantly, we decided to utilize structs in MATLAB to store the design parameters in our software. The `aircraft` struct is first initialized in the code with substructs (e.g. `performance`, `mission`, `weight`, `aerodynamics`, etc.), each of which stores related parameters in one centralized location, including both user inputs and values generated by functions. The modular nature of structs allows for easy parametrization of the code. Consequently, we are able to quickly and dynamically re-design our aircraft by changing specific user-inputs, which produces a cascading effect in the rest of our code.

The DSM of our entire software package is pictured in Figure 25 below, displaying a high level overview of the parameters it calculates and how they feed into various functions.

Rows in orange represent user-input values/parameters. Rows in green represent parameters that are calculated and output from a custom-built function. Rows in blue represent parameters that are outputs of code blocks. A block filled in gray above the diagonal indicates an input. For example, *Initial Fuel Fraction Estimation* takes input *Mission Profile*. A block filled in gray below the diagonal indicates an output. For example, the output of *T/W and W/S Constraints*

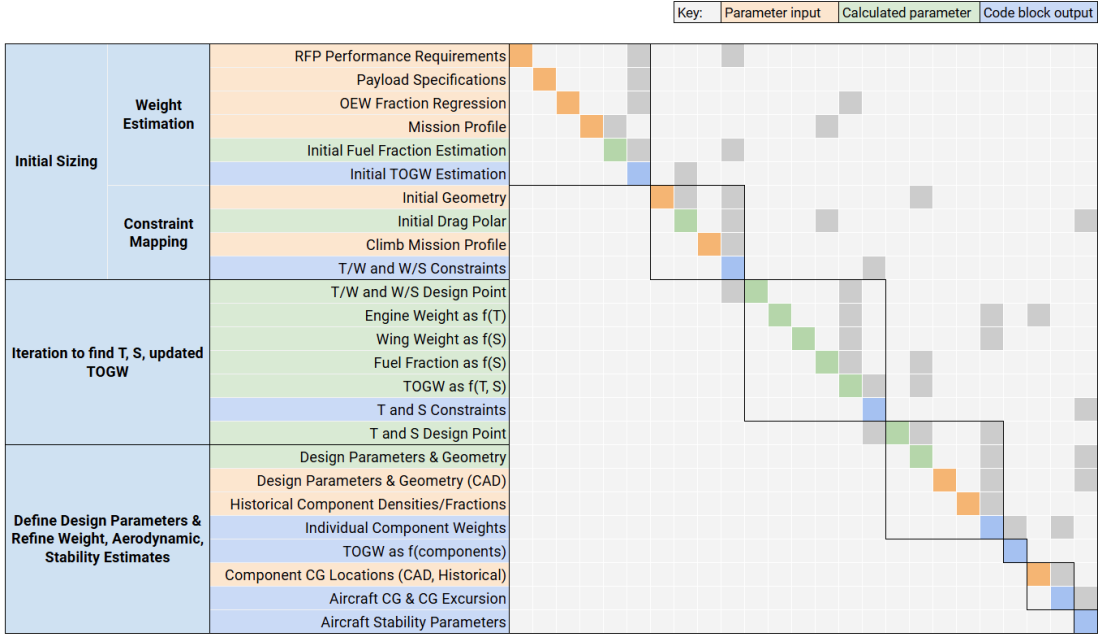


**Fig. 25 DSM for Libellula’s aircraft sizing software**

defines *T/W and W/S Design Point*. In the following sections, we will discuss each block in more detail.

#### A. Initialization, Initial TOGW Estimate, and T/W and W/S Constraint Mapping

To begin sizing our aircraft, it was necessary to make a preliminary estimate of our TOGW, which would inform the following design decisions and parameter definitions.

We start by populating our `aircraft` struct with known values. These include performance requirements, payload specifications, and mission profiles indicated by the RFP, in addition to an OEW fraction regression (equation 40), provided as courtesy by collaborating defense contractor Sainristil Defense.

Calculating the fuel fraction was a result of the input mission profile, historical fuel fraction values for specific mission segments, and the Breguet Range Equation. Plugging this fuel fraction (for the DCA mission, the most demanding), our OEW fraction regression, and our payload weight into our TOGW function and iterating, we were able to converge on a preliminary value of TOGW.

Initial geometric parameters were defined, namely the aspect ratio and wing sweep. We were then able to calculate our drag polar, estimating the Oswald efficiency factor  $e$  from Sartorius’s MATLAB function [22] which gives  $e$  as a function of wing sweep, aspect ratio and  $C_{D0}$ .  $C_f$ ,  $C_{D0 \text{ cruise}}$ , and  $C_L$  were determined from historical trends for similar aircraft, and  $C_{D0}$  was interpolated for takeoff and landing from delta values given by Roskam Table 3.6 [19].

Using this drag polar and historical values from Roskam [19], we were able to populate our mission struct with parameters for climb. Combining this with our geometric values and drag polar values, we found our *T/W and W/S constraint lines*, equations which can be found in section XV.A.

Finding constraint curves was a matter of plugging in an array of *T/W or W/S* values into the constraint equations

and plotting them over the appropriate regions. From this diagram, a design point was selected manually by observation, at the lowest  $T/W$  and highest  $W/S$  value within the feasible region. These plots and the selected design points are shown below. The feasible region is to the left of the landing field line, and above the specific excess power at 1g, SL line for both max and military thrust.

## B. Finding T, S, and Updated TOGW Estimate

These design points were subsequently used to produce a more refined estimate of TOGW. This new function takes input values of T and S, and has a few key differences from our initial weight estimate. Describing one iteration of a

- 1) Calculate the empty weight of the aircraft from a guess of TOGW using the regression from Equation 40.
- 2) Calculate the design parameters:
  - $S_{\text{design}} = \text{TOGW} \times (\text{selected design point } T/W \text{ ratio})$
  - $T_{\text{design}} = \text{TOGW} \times (\text{selected design point } W/S \text{ ratio})$
- 3) Adjust the empty weight using the input values of S and T:
  - Adjust for wing area:

$$\text{Adjustment for } S = (S_{\text{in}} - S_{\text{design}}) \times (\text{area density of wings})$$

- Adjust for thrust:
- $$\text{Engine weight adjustment} = \text{calculate engine weight for } T_{\text{in}} - T_{\text{design}}$$
- Add the engine weight adjustment to the empty weight.
- 4) Update the empty weight fraction with the new empty weight value.

With our empty weight now calculated, we make a refined estimate of the fuel fraction in a new function:

- 1) Determine  $S_{\text{wet}}$  using the regression from Equation 41 provided by Roskam Table 3.5 [19].
- 2) Calculate a new  $C_{D_0}$  using the input  $S_{\text{in}}$ .
- 3) Use the new  $C_{D_0}$  to determine  $L/D$ .
- 4) Use the refined  $L/D$  estimate in the Breguet Range equation to find the updated fuel fraction.

With these two fractions and the weight of our payload, we find TOGW and iterate until we converge on a value. Combining our new TOGW estimation with our  $T/W$  and  $W/S$  constraints, we are able to calculate T and S. For example, to calculate T given an value of  $S_{\text{in}}$ :

- 1) Take a guess of  $T$
- 2) Calculate TOGW as  $f(T, S)$
- 3) Calculate  $W/S$  from  $S_{\text{in}}$  and TOGW
- 4) Calculate  $T/W$  from the constraint equation and the new  $W/S$
- 5) Calculate the new  $T$  from  $T/W$  and the calculated TOGW
- 6) Iterate until converged.

The same was repeated to find S given a value for T and W/S constraints. This process was completed for each constraint over defined ranges of T and S to find our  $T - S$  plots.

### C. Refined Weight & Aerodynamic Estimates

After selecting  $T$  and  $S$ , we moved forward with selecting the rest of our values for our aircraft design, and began implementing them in CAD. From our CAD model, we were able to find the surface areas of various components. Combining this with historical values for weight densities/fractions of TOGW for various components, we were able to converge on a new estimate for TOGW using the following approach, provided by the metabook [3]:

- 1) Compute fuel fraction:  $\frac{W_f}{W_0}$
- 2) Compute fuel weight:  $W_f = \frac{W_f}{W_0} \times W_0$
- 3) Compute landing gear weight, a fraction of TOGW:  $W_{lg} = 0.043W_0$
- 4) Compute extra weight, a fraction of TOGW:  $W_{xtra} = 0.17W_0$
- 5) Compute the new MTOW:

$$W_{0new} = W_{engine} + W_{wing} + W_{ht} + W_{vt} + W_{fuse} + W_{xtra} + W_{lg} + W_f + W_{payload} + W_{crew}$$

- 6) Check for convergence
- 7) Update MTOW value:  $W_0 \leftarrow W_{0new}$

Using these individual component weights along with inputs of the CG positions of the components (which were pulled from CAD and MAC calculations for wing/stabilizer), we were able to calculate the overall CG of the aircraft. MATLAB's support of matrix math made finding the 3-dimensional center of gravity excursion relatively simple.

## XIII. Conclusions

In conclusion, while this design has reached a significant level of maturity for its current phase, our focus now shifts to towards refining our approach and enhancing our understanding our the aircraft's performance parameters. We are confident in our thrust-to-weight ( $T/W$ ) and wing loading ( $W/S$ ) constraints, as well as our takeoff gross weight (TOGW) estimations, which align with our mission requirements. Furthermore, we believe that the functions and capabilities defined in our design effectively address the operational needs of a homeland defense interceptor.

However, we recognize that the specific aerodynamic values we are currently utilizing may require further validation. As we refine our design, adjustments to these parameters may lead to changes in our overall design point, necessitating an iterative approach. Moving forward, our next steps will involve a thorough re-evaluation of the aerodynamic characteristics, including airfoil selection and performance testing. We will also expand our objective function method, gaining a more accurate estimate of cost that can inform our design decisions. By continually iterating on our design and integrating new insights, we aim to enhance the overall efficiency and effectiveness of our aircraft, ensuring it meets the demands of future operational scenarios.

## XIV. References

- [1] Raymer, D. P., *Aircraft Design: A Conceptual Approach*, AIAA Education Series, American Institute of Aeronautics and Astronautics, Inc., Reston, VA, 2018. URL <https://na01.safelinks.protection.outlook.com/?url=https%3A%2F%2Flccn.loc.gov%2F2018033769>.
- [2] Lutze, “AOE 3104 Course Materials,” , ???? URL <https://archive.aoe.vt.edu/lutze/AOE3104/>, accessed: 2024-10-27.
- [3] Martins, J. R. R. A., *The Metabook of Aircraft Design*, 2021. Compiled on Sunday 17<sup>th</sup> October, 2021 at 06:26.
- [4] Finck, R. D., *United States Air Force Stability and Control DATCOM*, McDonnell Douglas Corporation, 1978. URL <https://apps.dtic.mil/sti/pdfs/ADB072483.pdf>, accessed: 2024-10-25.
- [5] Gilruth, R. R., “Analysis and prediction of longitudinal stability of airplanes,” Tech. rep., NACA, 1941. URL <https://ntrs.nasa.gov/api/citations/19930091789/downloads/19930091789.pdf>, accessed: 2024-10-25.
- [6] Force, U. A., “F-16 Fighting Falcon,” , n.d.. URL <https://www.af.mil/About-Us/Fact-Sheets/Display/Article/104505/f-16-fighting-falcon/>.
- [7] Vietnam Warbirds Resource Group, “Lockheed F-104 Starfighter,” , 2024. URL <http://vietnam.warbirdsresourcegroup.org/f104.html>, accessed: 2024-10-24.
- [8] Güzelbey, H., Eraslan, Y., and Doğru, M. H., “Effects of Taper Ratio on Aircraft Wing Aerodynamic Parameters: A Comparative Study,” *European Mechanical Science*, Vol. 3, No. 1, 2019, pp. 18–23. <https://doi.org/10.26701/ems.487516>, URL <https://dergipark.org.tr/tr/download/article-file/629766>, accessed: 2024-10-24.
- [9] Scholz, D., “Aircraft Design - Part VII: Wing Design,” , 2021. URL [https://www.fzt.haw-hamburg.de/pers/Scholz/HOOU/AircraftDesign\\_7\\_WingDesign.pdf](https://www.fzt.haw-hamburg.de/pers/Scholz/HOOU/AircraftDesign_7_WingDesign.pdf), accessed: 2024-10-24.
- [10] Unknown, A., “Title Unknown,” *Munin Open Research Archive*, Year Unknown. URL <https://munin.uit.no/bitstream/handle/10037/6940/article.pdf?sequence=1>, accessed: 2024-10-24.
- [11] Embry-Riddle Aeronautical University, “Flying Fast,” , 2024. URL <https://eaglepubs.erau.edu/introductiontoaerospaceflightvehicles/chapter/flying-fast/>, accessed: 2024-10-24.
- [12] Embry-Riddle Aeronautical University, “Anatomy of Aircraft and Spacecraft,” , 2024. URL <https://eaglepubs.erau.edu/introductiontoaerospaceflightvehicles/chapter/anatomy-of-aircraft-and-spacecraft/>, accessed: 2024-10-24.
- [13] Hosseini, S. A., Shakiba-Hojjati, M., Ghiasi, H., and Khalkhali, A., “Aerodynamic Design and Analysis of Winglets,” , 2012. URL <https://core.ac.uk/download/pdf/11152406.pdf>, accessed: 2024-10-24.
- [14] Global Aircraft Organization, “J-7 Fishbed,” , 2024. URL [https://www.globalaircraft.org/planes/j-7\\_fishbed.pl](https://www.globalaircraft.org/planes/j-7_fishbed.pl), accessed: 2024-10-24.
- [15] Kasi, L., and Thangavelu, P., “Reducing Shock Wave Strength on Airfoil Surfaces with Nanomaterial Coating at Supersonic Speed,” 2024. URL [https://www.researchgate.net/publication/378703195\\_Reducing\\_Shock\\_Wave\\_Strength\\_on\\_Airfoil\\_Surfaces\\_with\\_Nanomaterial\\_Coating\\_at\\_Supersonic\\_Speed](https://www.researchgate.net/publication/378703195_Reducing_Shock_Wave_Strength_on_Airfoil_Surfaces_with_Nanomaterial_Coating_at_Supersonic_Speed), accessed: 2024-10-24.
- [16] Spreemann, K. P., “Technical Memorandum: NASA-TM-X-26,” Technical Memorandum (TM) NASA-TM-X-26, NASA Langley Research Center, Hampton, VA, United States, aug 1959. URL <https://ntrs.nasa.gov/search.jsp?R=19630003100>, document ID: 19630003100, Acquisition Source: Langley Research Center, Accession Number: 63N12976.
- [17] Hosseini, E., “CFD analysis of the aerodynamic characteristics of biconvex airfoil at compressible and high Mach numbers flow,” *SN Applied Sciences*, Vol. 1, 2019, p. 1283. <https://doi.org/10.1007/s42452-019-1334-2>.
- [18] Cinar, G., “AE481 Aircraft Design: Syllabus and Guide,” Compiled on Tuesday 10th September, 2024 at 15:35 UTC, 2024.

- [19] Roskam, J., *Airplane Design: Preliminary Sizing of Airplanes*, Roskam Aviation and Engineering Corporation, Ottawa, Kansas, 1985. First printing.
- [20] Ge, S. Y. X. L., C., “Design and Analysis of a Ventral Diverterless Supersonic Inlet,” *Journal of Physics: Conference Series*, Vol. 1985, 2021. <https://doi.org/10.1088/1742-6596/1985/1/012037>.
- [21] Tan, G. R., H., “Design and Wind Tunnel Study of a Top-mounted Diverterless Inlet,” *Chinese Journal of Aeronautics*, Vol. 17, 2004, pp. 72–78. [https://doi.org/10.1016/S1000-9361\(11\)60217-3](https://doi.org/10.1016/S1000-9361(11)60217-3).
- [22] S., S., “Oswald efficiency estimation function,” <https://www.mathworks.com/matlabcentral/fileexchange/38800-oswald-efficiency-estimation-function>, 2024. MATLAB Central File Exchange, Retrieved October 23, 2024.
- [23] Scholz, D., “Aircraft Design for HOOU,” <https://www.fzt.haw-hamburg.de/pers/Scholz/HOOU/index.html>, 2024. Open Educational Resource (OER) from Hamburg Open Online University.
- [24] Force, U. A., “F-35A Lightning II,” , n.d.. URL <https://www.af.mil/About-Us/Fact-Sheets/Display/Article/478441/f-35a-lightning-ii/>.
- [25] Force, U. A., “F-22 Raptor,” , n.d.. URL <https://www.af.mil/About-Us/Fact-Sheets/Display/Article/104506/f-22-raptor/>.
- [26] McGhee, R. J., and Beasley, W. D., “Low-Speed Aerodynamic Characteristics of a 17-Percent-Thick Supercritical Airfoil Design for General Aviation Applications,” Tech. Rep. NASA-TP-1538, NASA Langley Research Center, 1979. URL <https://ntrs.nasa.gov/api/citations/19790019972/downloads/19790019972.pdf>, accessed: 2024-10-24.

## XV. Appendix

### A. Constraint Equations

#### 1. $\frac{W}{S}$ Constraint from Landing Field Length

Gathered from Scholz, Section 5 Eqn. 5.5 [23]

$$\frac{m_{ML}}{S_W} = k_L \cdot \sigma \cdot C_{L,\max,L} \cdot (s_{runway} - s_a) \quad (17)$$

with  $k_L = 0.107 \text{ kg/m}^3$ .

$$s_{runway} = 8000 \text{ ft}$$

$$s_a = 1000 \text{ ft}$$

$$\sigma = \frac{\rho_{SL, 30^\circ C}}{\rho_{MSL}}$$

#### 2. $\frac{T}{W}$ Takeoff Field Length

From Roskam Section 3.9 [19]

$$\frac{T}{W} = \frac{1}{k_2} \left( \frac{k_1 \cdot \frac{W}{S_{in}} + BFL \cdot \rho_{SL, 30^\circ C} \cdot 0.72 \cdot C_{D0,TO}}{BFL \cdot \rho_{SL, 30^\circ C} \cdot C_{L,\max, TO}} + \mu_G \right) \quad (18)$$

with  $BFL = 8000 \text{ ft}$

$$k_1 = 0.0447$$

$$k_2 = 0.76$$

$$\mu_G = 0.03$$

$$C_{L,TO} = 1.7$$

### 3. $\frac{W}{S}$ Instantaneous Turn

From Raymer Section 5.3.9 [1]

$$n = \sqrt{\left(\frac{\psi V_{\text{corner}}}{g}\right)^2 + 1}, \quad (19)$$

$$q = \frac{\rho_{35000\text{ft}} \cdot (V_{\text{corner}})^2}{2} \quad (20)$$

$$\frac{W}{S} = \frac{q \cdot C_{L,\text{combat}}}{n} \quad (21)$$

$$v_{\text{corner}} = 155.556 \text{ m/s (550 km/hr)}$$

$$\psi = 18\text{deg/s (from RFP)}$$

### 4. $\frac{T}{W}$ Sustained Turn

From Raymer Section 5.3.9 [1]

$$n = \frac{1}{\cos(\theta_{\text{bank}})} \quad (22)$$

$$q = \frac{\rho_{35000\text{ft}} \cdot v_{\text{turn}}^2}{2} \quad (23)$$

$$T_W = \frac{q \cdot CD_0^{\text{clean}}}{\frac{W}{S} \cdot g} + \frac{n^2}{q \cdot \pi \cdot AR \cdot e_{\text{combat}}} \cdot \left(\frac{W}{S} \cdot g\right) \quad (24)$$

### 5. $\frac{T}{W}$ Cruise and Dash

From Aircraft Design Metabook Chapter 4.10 [3]

$$n = 1 \quad (25)$$

$$q_{\text{cruise}} = \frac{\rho_{35000\text{ft}} \cdot v_{\text{cruise}}^2}{2} \quad (26)$$

$$\frac{T}{W_{cruise}} = \frac{q_{cruise} \cdot CD_0^{\text{clean}}}{\frac{W}{S} \cdot g} + \frac{n^2}{q \cdot \pi \cdot AR \cdot e_{\text{cruise}}} \cdot \left( \frac{W}{S} \cdot g \right) \quad (27)$$

$$q_{dash} = \frac{\rho_{35000\text{ft}} \cdot v_{dash}^2}{2} \quad (28)$$

$$\frac{T}{W_{dash}} = \frac{q_{dash} \cdot CD_0^{\text{clean}}}{\frac{W}{S} \cdot g} + \frac{n^2}{q \cdot \pi \cdot AR \cdot e_{\text{supersonic}}} \cdot \left( \frac{W}{S} \cdot g \right) \quad (29)$$

## 6. $\frac{T}{W}$ Ceiling

From Aircraft Design Metabook Chapter 4.11 [[3]]

$$T_W = \left( \frac{\rho_c}{\rho_{SL}} \right)^{0.6} \cdot T_{SLS} \quad (30)$$

$$\frac{T}{W} = \frac{1}{\left( \frac{\rho_c}{\rho_{SL}} \right)^{0.6}} \cdot (G + 2\sqrt{\frac{C_{D0}}{\pi A Re}}) \quad (31)$$

## 7. $\frac{T}{W}$ Climb

From Aircraft Design Metabook Chapter 4.7 [3]

$$\frac{T}{W} = \frac{(K_s)^2}{C_{L,\text{max}}} \cdot C_{D0} + \frac{C_{L,\text{max}}}{(K_s)^2 A Re} + G \quad (32)$$

$$\left( \frac{T}{W} \right)_{takeoff} = \left( \frac{1}{0.8} \right) \cdot \left( \frac{1}{0.94} \cdot \left( \frac{N_{\text{engine}}}{N_{\text{engine}} - 1} \right) \cdot \left( \frac{W}{W_{\text{takeoff}}} \right) \cdot \left( \frac{T}{W} \right) \right) \quad (33)$$

## 8. $\frac{T}{W}$ Specific Excess Power

From Raymer Textbook Chapter 7 [1]

$$P_{SE} = \frac{T - D}{W} \cdot V \quad (34)$$

$$\frac{W}{S_{50\%fuel}} = \frac{W}{S_{N/m^2}} \cdot \frac{(1 + (1 - ff))}{2} \cdot n \quad (35)$$

$$q_{dash} = \frac{\rho \cdot v^2}{2} \quad (36)$$

$$C_L = \frac{\frac{W}{S} \text{50\%fuel}}{q} \quad (37)$$

$$C_D = C_{D_0} + \frac{C_L^2}{\pi \cdot AR \cdot e} \quad (38)$$

$$\frac{T}{W_{SEP}} = \frac{P_s}{v} + \frac{qC_D}{\frac{W}{S} \text{50\%fuel}} \quad (39)$$

## B. Additional Equations

### 1. Empty Weight Fraction Regression

$$\frac{W_e}{W_0} = 0.882 \cdot W_0^{-0.055} \text{ (lbm)} \quad (40)$$

### 2. $S_{wet}$ from TOGW Regression

$$S_{wet} (\text{ft})^2 = 10^{-0.1289} \cdot W_0^{0.7506} \quad (41)$$

## C. Additional Plots

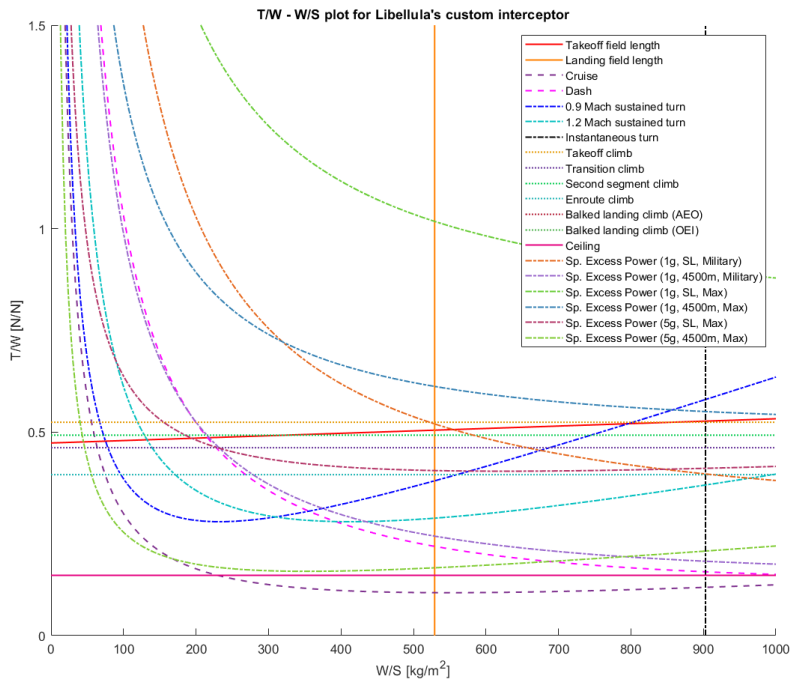


**Fig. 26** *T/W – W/S Plot, All Constraints Together*

#### D. Wing Parameters

[h!]

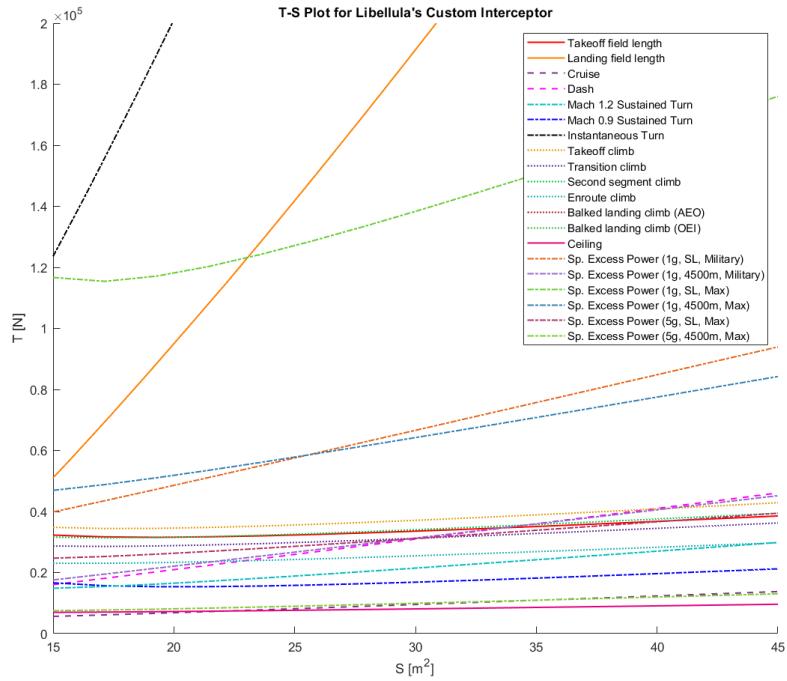


**Fig. 27**  $T - S$  Plot, all constraints

## E. Wing Design

**Table 11** Values of  $e$  for Different Aircraft Configurations

Configuration	$e$
Cruise	0.881
Takeoff Flaps	0.853
Landing Flaps	0.747
Supersonic	0.500

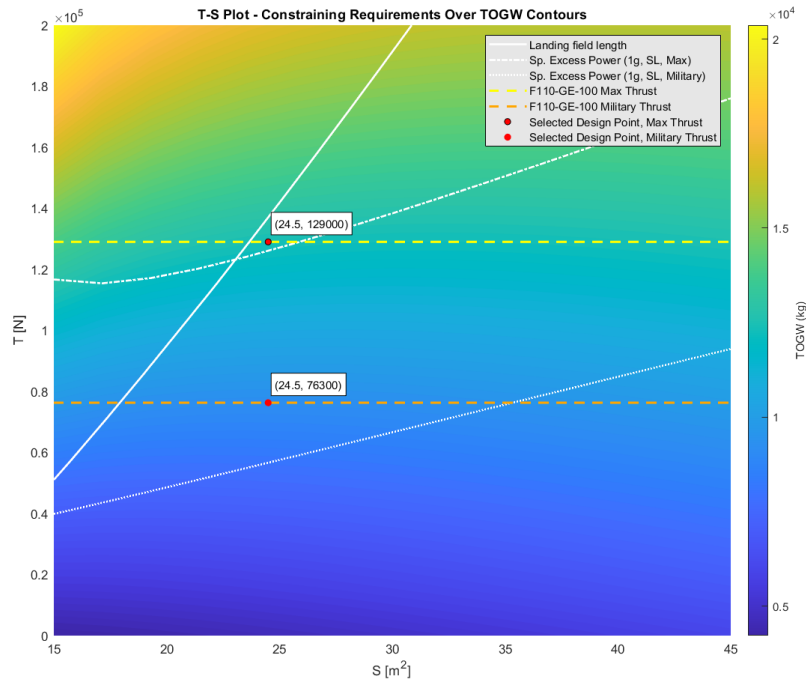


**Fig. 28**  $T - S$  Plot, constraining lines plotted over TOGW contours

**Table 12** Values of  $C_{D_0}$  for Different Aircraft Configurations

Configuration	$C_{D_0}$
Clean	0.024
Takeoff Flaps	0.034
Takeoff Flaps + Gear	0.049
Landing Flaps	0.079
Landing Flaps + Gear	0.094

## F. Empennage Design

$$\Delta C_{D_{0\text{flap}}} = F_{\text{flap}}(C_f/C)(S_{\text{flapped}}/S_{\text{ref}})(\delta_{\text{flap}} - 10) \quad (12.61)$$

where

$\delta_{\text{flap}}$  = in degrees

$F_{\text{flap}}$  = 0.0144 for plain flaps = 0.0074 for slotted flaps

$C_f$  = chord length of flap (see Fig. 12.18)

$$\Delta C_{D_i} = k_f^2(\Delta C_{L_{\text{flap}}})^2 \cos \Lambda_{\bar{c}/4} \quad (12.62)$$

**Fig. 29 Equations From Raymer Used for Flap Sizing**

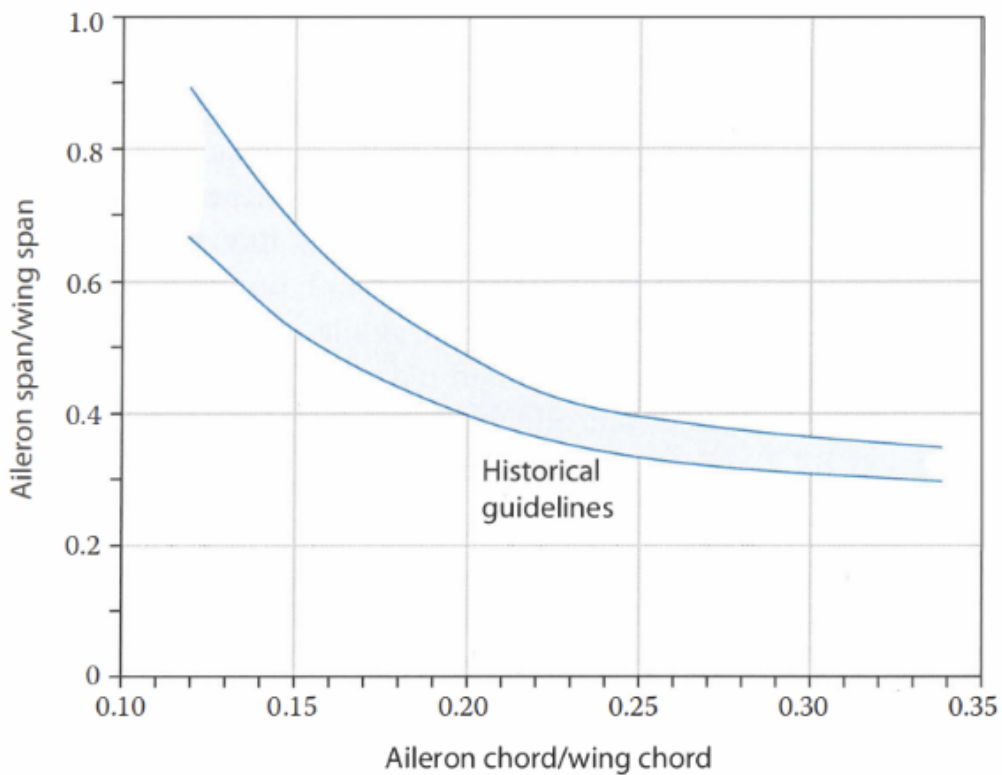


**Fig. 30 Chart in Raymer Used for Aileron Sizing**

[h]

**Fig. 31 Overall Sizing of Flaperons**

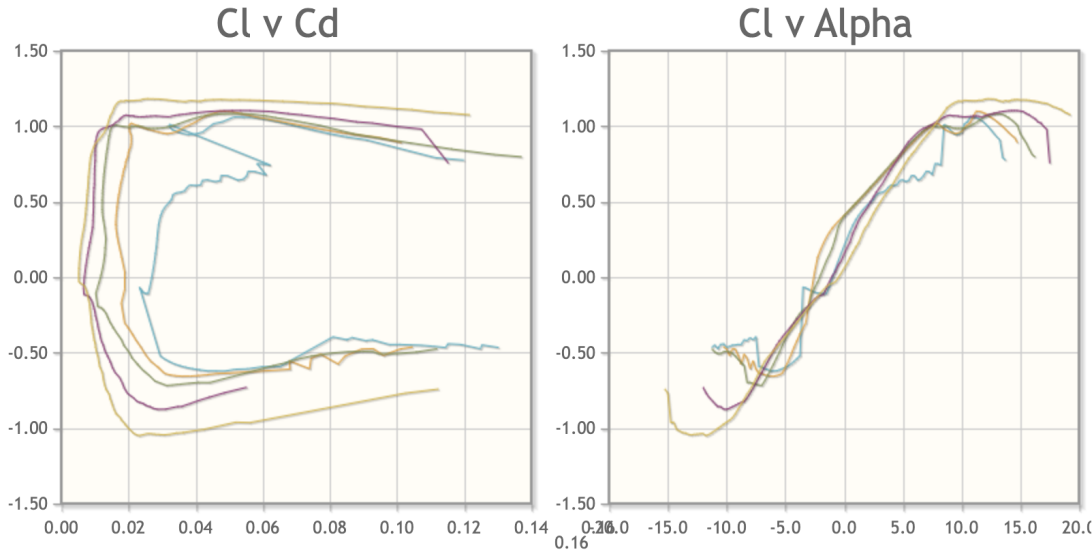


**Fig. 32** Drag Polar and  $C_L$  Alpha Graph for the TsAGI S-12 Airfoil

**Table 13** Values of  $C_L$  for Different Aircraft Configurations

Configuration	$C_L$
Cruise	1.25
Takeoff Flaps	1.70
Landing Flaps	2.00
Combat	1.00

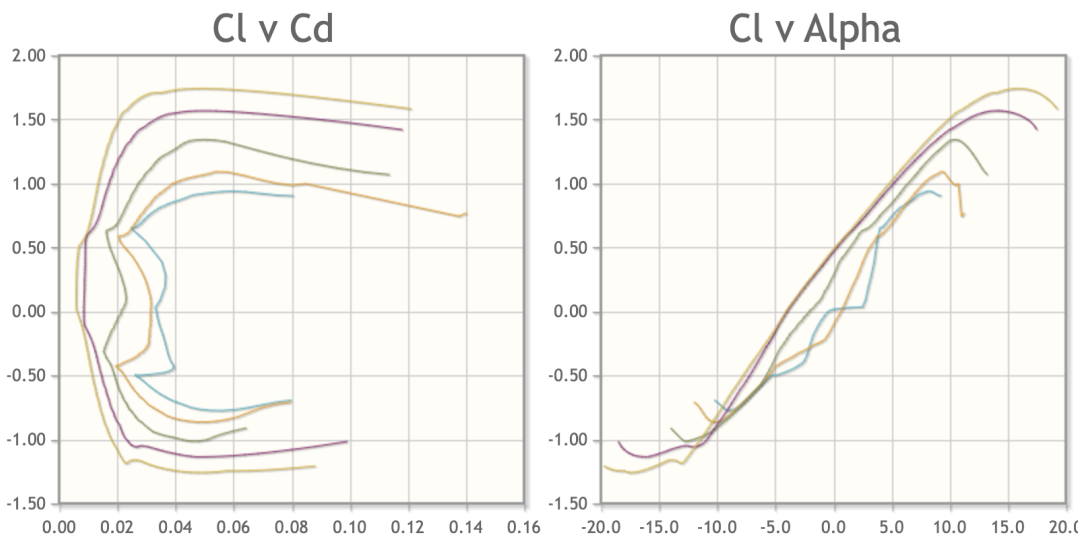


**Fig. 33** Drag Polar and  $C_L$  Alpha Graph for the NASA SC(2)-0.614 Airfoil

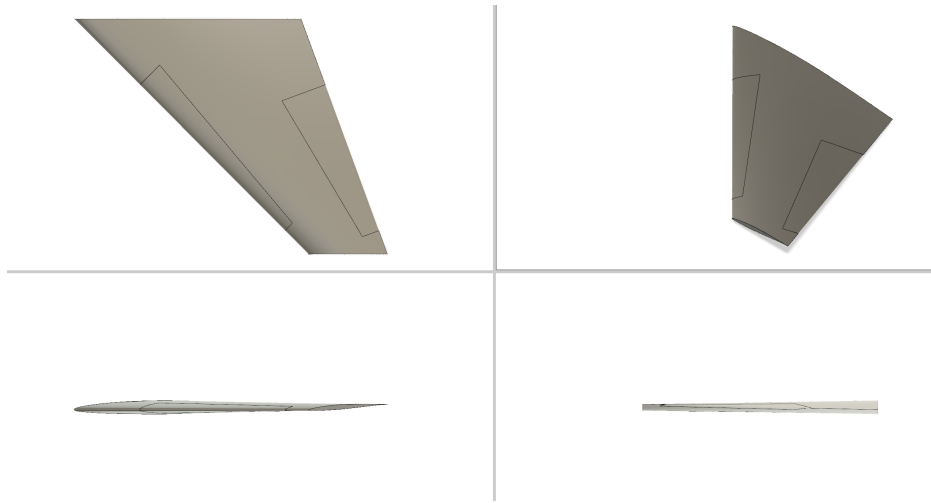


**Fig. 34 4-View CAD of Wing Design**

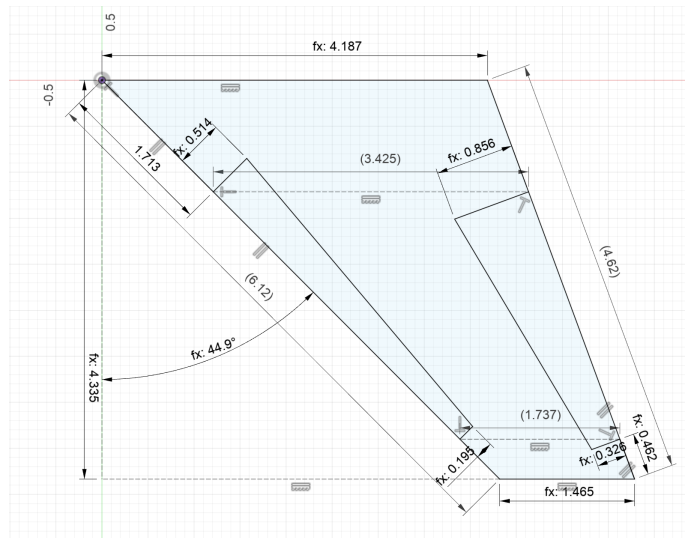


**Fig. 35 Top-View of Wing Design with Labeled Dimensions and Parameters**

**Table 14 Values of  $C_D$  for Different Aircraft Configurations**

Configuration	$C_D$
Cruise	0.208
Takeoff Flaps	0.385
Takeoff Flaps + Gear	0.400
Landing Flaps	0.634
Landing Flaps + Gear	0.649

**Table 15** Values of  $L/D$  for Different Aircraft Configurations

Configuration	$L/D$
Max Cruise	9.46
Cruise	6.02
Max Takeoff Flaps	7.82
Takeoff Flaps	4.42
Max Takeoff Flaps + Gear	6.50
Takeoff Flaps + Gear	4.25
Max Landing Flaps	4.79
Landing Flaps	3.15
Max Landing Flaps + Gear	4.39
Landing Flaps + Gear	3.08

**Table 16** Values of Air Density ( $\rho$ ) for Different Conditions

Condition	$\rho$ (kg/m <sup>3</sup> )
SL at 30°C	1.164
35,000 ft	0.379
MSL	1.088

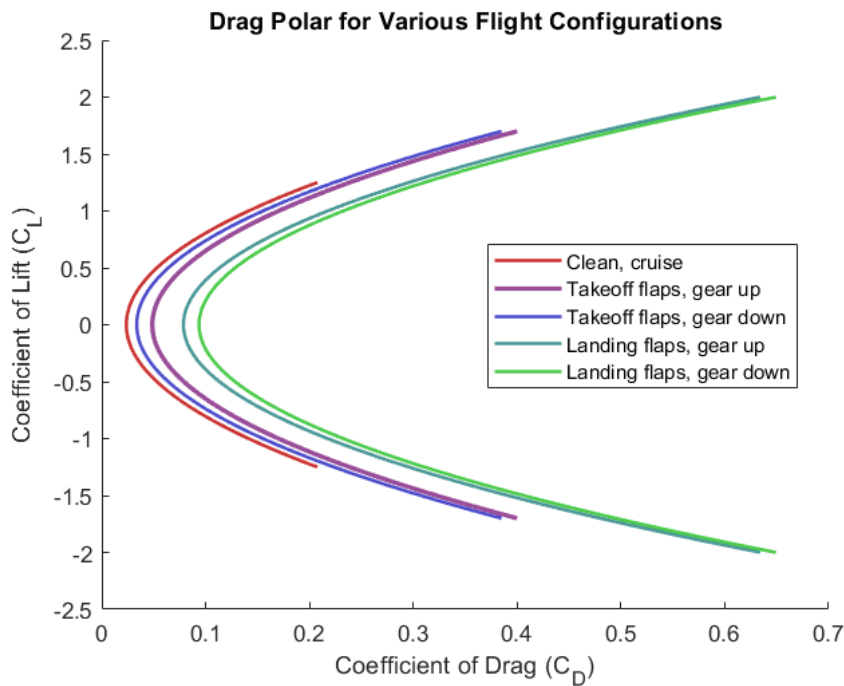


**Fig. 36** Preliminary Drag Polar for Our Aircraft

**Table 17 Summarized Empennage Parameters**

Parameter	Vertical Tail	Horizontal Tail
Single Surface Reference Area	$0.8695 \text{ m}^2$	$1.8303 \text{ m}^2$
Single Surface Span	$0.9325 \text{ m}$	$1.9133 \text{ m}$
Root Chord	$1.3815 \text{ m}$	$1.2755 \text{ m}$
Tip Chord	$0.4835 \text{ m}$	$0.6378 \text{ m}$
Aspect Ratio	2	4
Sweep ( $\Lambda$ )	$55^\circ$	$49.9^\circ$
Taper ( $\lambda$ )	0.35	0.5
Airfoil Shape	Biconvex	Biconvex
Max Thickness to Chord Ratio ( $\frac{t}{c}_{max}$ )	3.3%	3.3%
Location of $\frac{t}{c}_{max}$	$0.5c$	$0.5c$
Low Speed Lift Curve Slope ( $\frac{\partial C_L}{\partial \alpha}$ )	$0.067 \text{ rad}^{-1}$	$0.067 \text{ rad}^{-1}$
Transonic Lift Curve Slope ( $\frac{\partial C_L}{\partial \alpha}$ )	$0.077 \text{ rad}^{-1}$	$0.077 \text{ rad}^{-1}$
Supersonic Lift Curve Slope ( $\frac{\partial C_L}{\partial \alpha}$ )	$0.073 \text{ rad}^{-1}$	$0.073 \text{ rad}^{-1}$
Incidence Angle	-	-

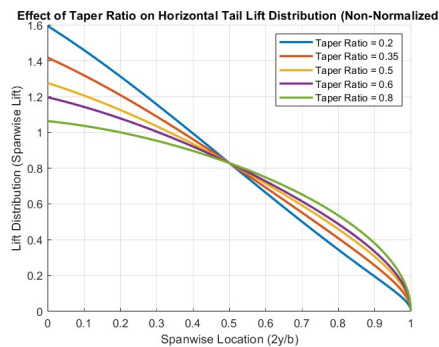


**Fig. 37 Non-Normalized Lift Distribution on Horizontal Tail with Varying Taper Ratios**

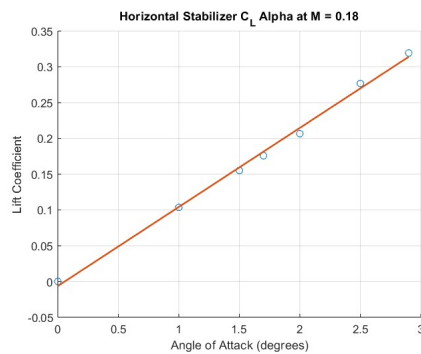


**Fig. 38 Lift Curve Slope from NACA 0003 mfoil Simulations at Take-Off Mach**

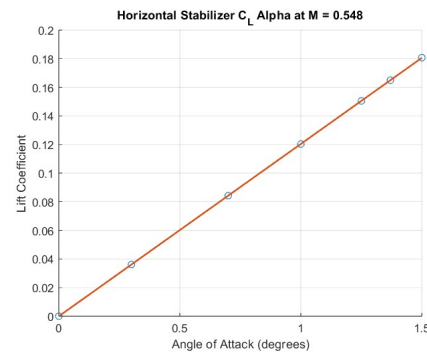


**Fig. 39 Lift Curve Slope from NACA 0003 mfoil Simulations at Cruise Mach**

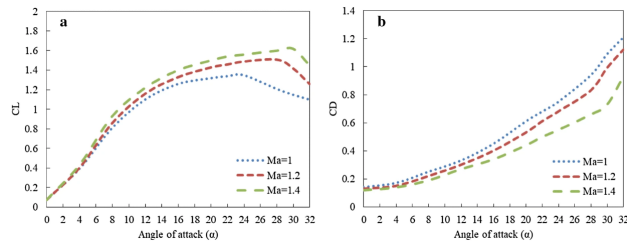


**Fig. 40 Lift Curve Slope from Biconvex Airfoil CFD Simulations Performed by Hosseini [17]**

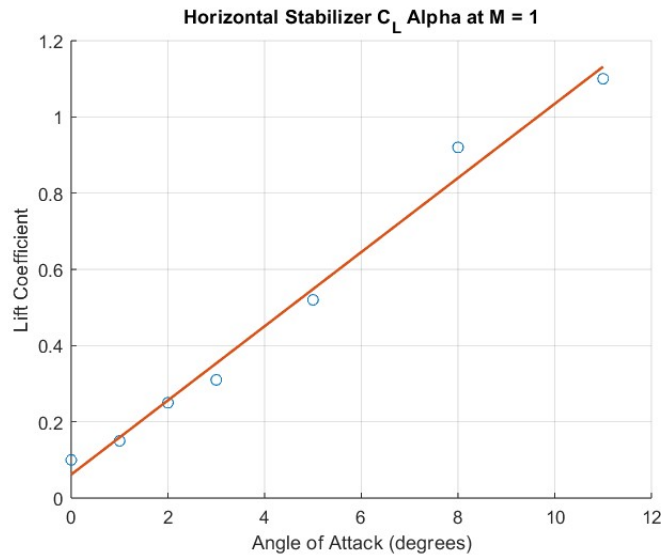


**Fig. 41 Lift Curve Slope Regression from Hoseini [17] CFD Data Linear Segment at M = 1**

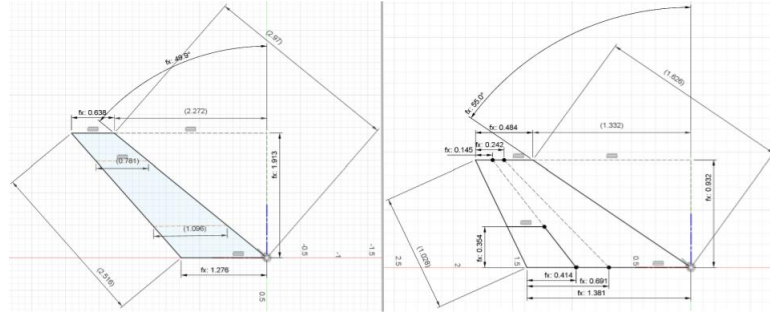


**Fig. 42** Horizontal Tail [Left] and Vertical Tail [Right] Dimensions

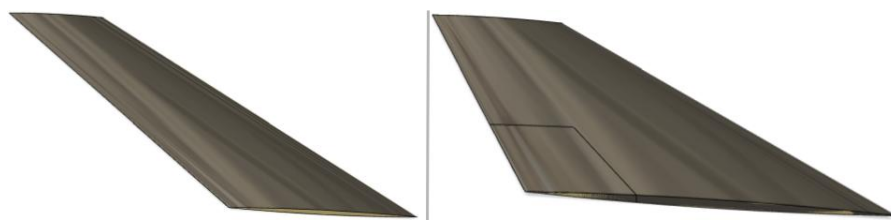


**Fig. 43** Horizontal Tail [Left] and Vertical Tail [Right] 3D Render